

國立臺灣大學理學院地質科學研究所

碩士論文

Department of Geosciences

College of Science

National Taiwan University

Master thesis

2005 年宜蘭雙主震之震源機制解：

應用近場波形反演法探討區域地震機制

**The Ilan Earthquake Pair on 5 March 2005:
Discussion on Focal Mechanism Determination
with Near-field Waveform Inversion**

王天慧

Tien-Huei Wang

指導教授：吳逸民 博士

張道明 博士

Advisor: Yih-Min Wu, Ph.D.

Tao-Ming Chang, Ph.D.

中華民國 九十六 年 六 月

June, 2007

國立臺灣大學
地質科學研究所

碩士論文

2005 年宜蘭雙主震之震源機制解：
應用近場波形反演法探討區域地震機制

王天慧
撰

國立臺灣大學碩士學位論文
口試委員會審定書

2005 年宜蘭雙主震之震源機制解：
應用近場波形反演法探討區域地震機制
The Ilan Earthquake Pair on 5 March 2005:
Discussion on Focal Mechanism Determination
with Near-field Waveform Inversion

本論文係王天慧君 (R94224203) 在國立臺灣大學理學系、
所完成之碩士學位論文，於民國九十六年六月十五日承下列考
試委員審查通過及口試及格，特此證明

口試委員：

吳逸民

(簽名)

(指導教授)

黃柏壽

張道明

張林興

陳丁高

ACKNOWLEDGMENT

誌謝

很高興能下筆至此，整本論文的進度之中，就屬誌謝安排在最後一部份。寫到這裡，心中已充滿種種實在的感激，總覺得自己的努力是如此渺小，由無數身邊的人的幫助、照顧、提攜，才能好好地將這本論文完成。很像過去讀過陳之藩的“謝天”中所述：「要感謝的人太多了」。但我並不打算就以謝天帶過。

首先要感謝的，與一般人並無不同，卻也無可厚非的，是一直以來給予我最深的信任、無悔支持的父母。在你們的眼中，我是讓你們放心的孩子，也是因為你們給我很多空間和不斷的相信與關懷。再來，很感謝地震學研究室——我的指導教授 吳逸民老師，當時在研究室初成立時，就收容了對實務觀測還不熟悉，但很有興趣的許多大學部學生，讓我們有高水準的資料和資源可以進入地震學的領域，後來在碩士二年的生活中，無論是對研究還是人生，持續且耐心地為我們開導。在學習的過程中，您表現了強韌且高挑戰性的工作和人生觀，但卻總予我們獨立思考和決策的最大空間，讓我們正面、自由地去面對自己的決定，實際走出不同個人風格的路。之於研究的各種資源上，卻總是給我們最快也最多的支持，從您身上我學習到的，實在難以以幾句話盡述。還有，非常感謝 張道明老師在技術上的指導幫助，總是細心且沉穩地解答我的各種問題，提點我想法上的盲點，並適時鼓勵、告訴我在研究上不要心急。也感謝引領我進入地球物理領域的郭本垣老師，若不是有您，我也不會進入地球物理的世界，過著精彩的研究生活。謝謝 洪淑蕙、龔源成及 喬凌雲老師深入淺出的課程，在理論方面為學生們奠基。還有 陳于高老師這一年來的照顧，您把學生視為第一優先的領導精神，讓我們感到無限的溫暖和感動，也激起我們想更堅持科學這條路的精神。

在生活中，就像時時刻刻身處於超級星光大道的星光幫，每個在這裡的人都身懷絕技，且互相有著深厚的感情。有像研究室裡大姐姐一樣總是關心著我們的助理宜芬、亦師亦友、不吝於連我論文都要幫忙改，甚至是聽吐苦水的真男人阿和、會玩、會唱、懂生活，帶動著研究室，能夠透徹地分析指出我研究定位上的盲點，在工作時卻也是一把罩的信樺、不時出現的溫馨大師姐心儀，還有學弟妹 郁梅、秉延、芳儒、毓軒。並肩繼續作戰的戰友阿狗、小猛、珀儂。總愛一起討論研究想法、技術、音樂與旅遊的學長孟涵，聽過我無數遍報告演練的學姐酷酷狸，在寫論文期間陪我夜裡不閤眼的蠻牛學長和鈞元學弟，還有黃鐘、佳漢、欣穎學姐、咪咪、貼心的筱婷、童忻、詠恬，我經常去請教的蛋哥、鴉哥和 Ray，以及大學以來那些貼心的朋友們。忍受我在壓力時的種種情緒，總是想辦法逗我開心、叮囑我要成長的江透抽，有你們在身旁互相幫助、互相鼓勵，陪伴著我的碩士生生涯，實在是我永遠珍惜的時光。希望往後的路程上，可以帶著這些相伴的勇氣一起前行。

CONTENT

Acknowledgement	iii
Abstract	v
中文摘要	vi
List of Figures	viii
List of Tables	ix

1. Introduction i

1.1 Motivation and Goal	1
1.2 Study Strategy and Overview.....	6
1.3 Local Geological Background.....	7
1.4 Previous Studies, Comments and Debates	11
1.4.1 Seismic Reflection	11
1.4.2 Seismotectonic studies from first motion focal mechanism.....	12
1.4.3 Inversion Centroid Moment Tensors	15

2. Method and Theory 18

2.1 First Motion Focal Mechanism Determination.....	18
2.2 Moment Tensor Solution --Theory	19
2.2.1 Hypothesis	19
2.2.2 Green's Function and Synthetic.....	22
2.2.3 Inversion	24
2.3 Synthetic Seismogram Computation.....	27
2.3.1 Wave Integration.....	27
2.3.2 Source Time Function.....	27
2.3.3 Phase	28
2.4 Wave Integration and Correction	29
2.5 Single Station Approach	29
2.6 Multi-station Approach.....	30

3. Data and Material..... 32

3.1 Central Weather Bureau Seismic Network (CWBSN) Earthquake Catalogue	32
3.2 Taiwan Strong Motion Instrumentation Program (TSMIP) Strong Motion Station	33
3.3 One Dimension Velocity Model	37
3.4 Waveform Data.....	41
3.5 Synthetic Seismogram Computation.....	42

4. Results.....	43
4.1 <i>First Motion Solution and Local Aftershocks</i>	43
4.2 <i>Moment Tensor Solution—Single Station Result</i>	45
4.3 <i>Moment Tensor Solution—Multi-Station Result</i>	47
5. Discussions	52
5.1 <i>Single Station Inversion</i>	52
5.1.1 <i>Tradeoff Problem</i>	52
5.1.2 <i>Sensibility to Velocity Model</i>	54
5.1.3 <i>Solution to Single Station Problem</i>	55
5.2 <i>Multi-Station Inversion</i>	56
5.2.1 <i>Depth Test</i>	57
5.2.2 <i>Comparison with BATS</i>	60
5.2.2.1 <i>Focal Depth</i>	60
5.2.2.2 <i>Station Coverage</i>	60
5.2.2.3 <i>Velocity Model and Frequency Range</i>	61
5.3 <i>Local Clustered Aftershocks</i>	65
5.4 <i>Physical Interpretation for First Motion and Waveform Inversion</i>	68
5.5 <i>Local Earthquake Characteristics</i>	70
6. Conclusions	72
7. REFERENCES.....	73
8. APPENDIX.....	78
I. <i>CPS 3.3.0 application flow chart</i>	
II. <i>TSMIP site and instrument classification</i>	
III. <i>Bilingual words and Terminology</i>	

ABSTRACT

On 5 March 2005, an earthquake pair occurred at Ilan (121.84°E, 24.66°N), northeastern Taiwan. Both mainshocks have similar magnitude ($M_L = 5.9$ and $M_L = 6.0$). The first one was determined as a normal solution based on first-motion polarities of P wave from Central Weather Bureau Seismic Network (CWBSN) and Taiwan Strong Motion Instrumentation Program (TSMIP), while it was solved as a strike-slip solution by Broadband Array in Taiwan for Seismology (BATS) Centroid Moment Tensor (CMT) inversion. Normal faulting would be consistent with the opening and extension of Okinawa Trough on tectonic basis. On the other hand, a strike-slip solution would provide us one possible answer to the slip accommodation of compression. Thus, obtaining one reliable solution to this focal mechanism has become one important issue.

To resolve the focal mechanism mentioned above, we target the first mainshock for its solution inconsistency in two methods. Firstly we applied Moment Tensor Inversions using much denser TSMIP strong motion array in Ilan region. The kernel computer code was adopted from R. B. Herrmann (1985) and later modified by Huang (1994) and Chang (2005). Synthetic waveform is generated with wavenumber integration method to simulate the three-component time history from hypothesized point source. Results from 23 stations using single station approach suggest that lateral variance of velocity structures underneath Ilan plain are dramatic.

Multi-station inversion helped us to model this event at threshold magnitude ($M_L = 5.9$) as point source. It serves to cancel out velocity variances from each station. We further applied multi-station approach to conceal velocity variation along different paths. The inversion result from fifteen stations provided a more convincing, averaged slip solution. This event was an oblique event in between normal component and strike-slip. The first motion solution simply presents initial rupture motion of an event, which could

be irrelevant to subsequent slip motion of the whole cluster. By our result, we can conclude the initial rupture motion to be normal, and later strike-slip motion dominated the rest of this event. The multi-station approach is applicable for near-field TSMIP records to obtain reliable CMT solutions.



中文摘要

宜蘭雙主震發生於 2005 年 3 月 5 日(東經 121.84 度, 北緯 24.66 度), 第一主震深度為 10.54 公里, 在 19:06 分發震, 1.08 分鐘後第二主震又在深度 6.2 公里處發震。兩主震發生時間及位置都十分相近, 故一般合稱為雙主震。此雙主震由中研院台灣寬頻地震(BATS)所發布之波形反演地震斷層機制解, 兩者均判定為左移之走向滑移斷層, 但在氣象局(CWBSN)由 P 波初動解出的斷層機制解, 第一主震則為東北-西南走向之正斷層。此處震源之爭議點在於其可能的構造意涵而引發學界關注, 由於宜蘭平原向來被認知為台灣東部構造連接至沖繩海槽張裂帶的轉換, 且為沖繩海槽的向西延伸, 目前論述與模型繁多。而清楚底定雙主震之破裂機制, 因其特殊位置, 正可助於釐清關於構造轉換點的問題, 又單就其一主震, 有機會進一步探討制定地震斷層機制解在方法上的差異。

本研究中我們針對宜蘭雙主震的第一主震, 以兩種方法結果做比較。由於加上在宜蘭平原上密布之台灣強地動網陣列(TSMIP), 一方面有更精確的 P 波初動解, 另一方面可對加速度積分之地表位移做區域性的波形反演測試。據詳細理論方法的推斷, 以及配合餘震叢集的結果, 我們認為兩種方法呈現不同的地震破裂意涵。P 波初動只使用地震波中最初波相所具有的訊息, 表現了斷層初始破裂的運動, 而波形反演則使用完整波形的訊息, 代表了整個破裂過程平均的運動。因此, 兩種不同方法所得地震斷層面解有所差異, 是印證理論及反應此地震的區域特性的結果。

另外, 在區域波形反演方面, 我們延用 R. B. Herrmann(1985), 並由黃柏壽(1994)和張道明(2005)修改之波數積分法產生合成波形。首先以平原上 23 個測站單站波形擬合, 發現單站無法配合此區域側向上速度模型的不確定性, 使得反演結果並不穩定, 因而改以 15 個測站共同反演, 並且引用吳逸民(2007)最新台灣區域的地震層析成像(tomography)結果, 截取宜蘭地區平均的一維速度模型, 並加上宜蘭平原下低速層的區域構造。多站反演結果顯示, 共同反演確實可以得到較

為可信的斷層機制解。即使降低了各站波形的擬合度，多站反演出的單一解其穩定性、及與餘震之斷層機制解對比，仍表現出較合理的特性。根據本研究的結果，此一主震應為帶有正斷層分量之左移走向斷層。由這個證據應可推估，張裂與走向滑移的轉換點，最可能發生在宜蘭平原此一位置。



LIST OF FIGURES

1	First motion solution for the first mainshock.....	2
2	First motion solutions for the second mainshock.....	2
3	BATS CMT solution for two mainshocks.....	4
4	Station distribution of BATS and TSMIP array for two mainshocks.....	5
5	Flow chart of study procedure.....	7
6	Geological Map of Ilan region.....	9
7	Basement subsurface contour map with Active fault.....	10
8	Fault system from seismic reflection.....	11
9	Shallow Seismicity and Earthquake clusters for Ilan region.....	13
10	First motion focal mechanisms for Ilan region.....	14
11	Shape of source time function.....	28
12	TSMIP stations with classifications of site.....	34
13	TSMIP instrument response.....	36
14	TSMIP stations used in our study.....	37
15	Selected Tomography grids in Ilan region.....	39
16	Acceleration waveform from station ILA042.....	42
17	First motion result of five Aftershocks.....	44
18	Single station approach result.....	45
19	Station distribution for multi-station approach.....	48
20	Multi-station approach result.....	49
21	Multi-station approach waveform fit (I).....	50
	Multi-station approach waveform fit (II).....	51
22	Schematic example of inversion trade-off.....	53
23	Misfit and CLVD curve for the depth test.....	58
24	Solution variations for the depth test.....	59
25	Station coverage comparison.....	61
26	Velocity models comparison(0~50 km depth).....	62
27	Velocity models comparison(0~20 km depth).....	63
28	Two tomography profiles.....	64
29	Aftershock distribution and simulated fault plane.....	66
30	Five Aftershock distribution and pattern.....	68
31	Eight examples of local earthquake pattern.....	71

LIST OF TABLES

Table.1	Averaged tomographic velocity model for Ilan region.....	39
Table.2	Modified one-dimension velocity model.	40
Table.3	Parameters for single stations and inversed results.....	46
Table.4	The Focal depth test results and parameters.....	59



1. Introduction

1.1 *Motivation and Goal*

Focal mechanism has been used in geological interpretations to explain earthquake source as well as related tectonic. However, as a kind of tool, we need more precise understanding of: 1) the techniques to determine it, and 2) limits or advantages on application, and 3) its physical meaning. From a case at the Ilan region, we have now discovered that different approaches may have different results.

Intriguing example like this was noticed at seismological and seismotectonic studies until recent years. Much debate aroused from the true focal mechanism of the Ilan earthquake pair, which resided in the conjunction of subduction area. It involves NEE direction opening of Okinawa Trough, NS adjusting slip and NW-SE compression from Luzon island arc collision. On 5 March, 2005, at 19:06:52.12PM ($M_L = 5.9$, and depth 9.84 km) the first mainshock occurred, and then next mainshock ($M_L = 6.0$, and depth 9.52 km) followed in 1.08 minutes. It was reported by first motion solution that the first event was normal faulting (Fig.1). This implied that earthquake seismogenic zone may correlate to extension opening of Okinawa Trough. However, the first and second mainshock focal solutions from local moment tensor inversion (BATS) system

preferred left-lateral strike slip (Fig.3).

It left us puzzling on the fact of this event. The high density TSMIP array on Ilan plain suggests us better constraint on data quality for near field accelerograph. And, current new

tomography result obtained from denser seismicity and stations (Wu et al., 2007)

would also support our trail study for better Green's function constraint. For the second mainshock, the TSMIP data is insufficient to resolve a reliable first motion record. Thus we will emphasis on the first mainshock.

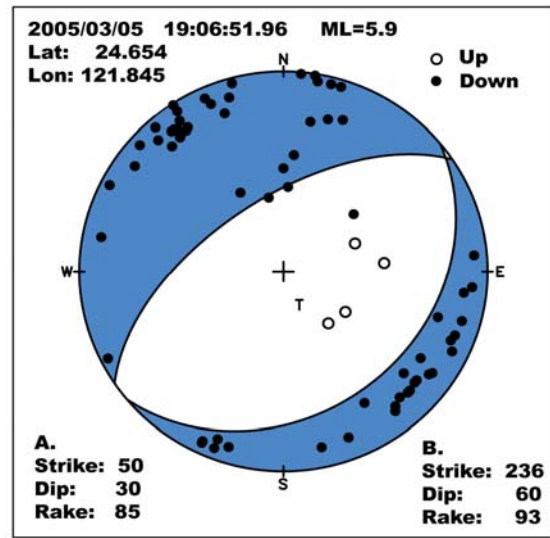


Fig.1 P wave first motion solution for the first mainshock, 5 March 2005, combined with TSMIP station records.

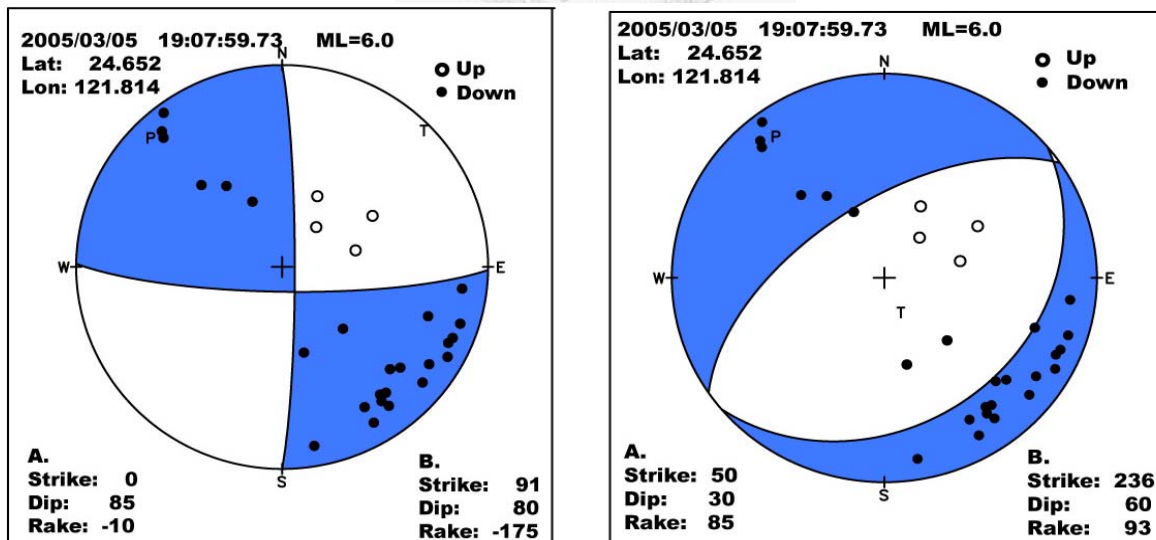
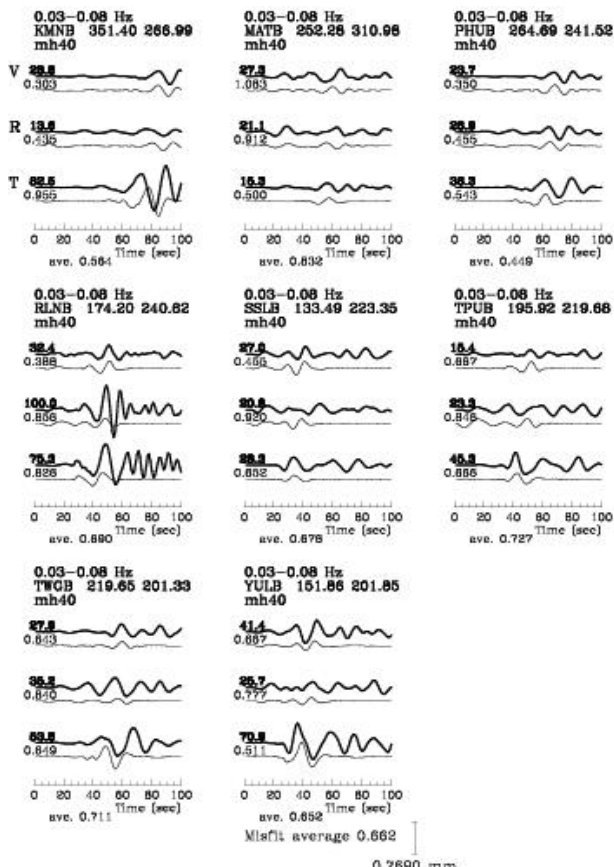


Fig.2 P wave first motion solution for the second mainshock, 5 March 2005, combined with TSMIP station records. This solution lacked data value on the fourth quadrant. The data had ambiguity on the solution. Left panel demonstrated the left lateral strike-slip, and right panel demonstrated normal the same with the attitude shown in figure 1.

We would hereby aim at the Ilan area and the first mainshock due to fine constraint on first-motion focal mechanism solution (Fig. 1). We would explain all possible effects technically and theoretically involved in two kinds of focal mechanism determination. Through this process, we can explore the reasons causing the differences on solutions. Under consideration of previous research (Liang et al., 2005; Tsao, 2006), we would work on two sides of evidence through experiments, and finally make our conclusion in this study. For specific strategy please refer to Chapter 1.





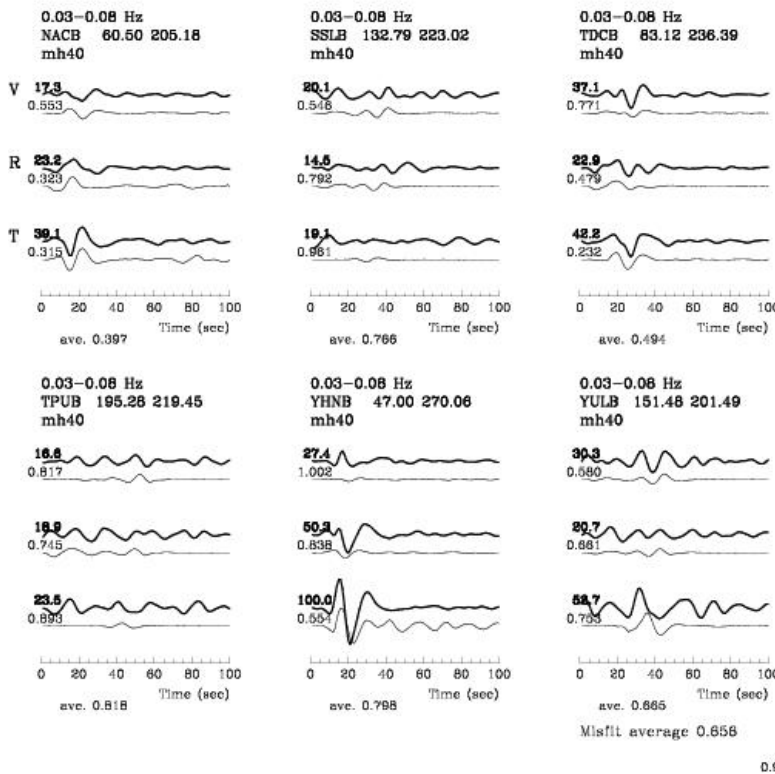
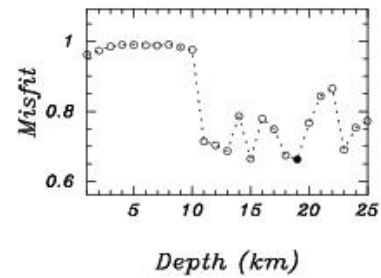
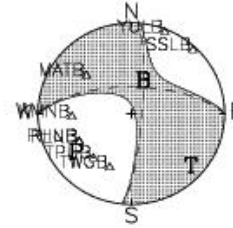
05/ 3/ 5 19: 6:51.60

(24.6700, 121.8500)

Depth= 19 km Mw = 5.51

Strike Dip Slip
Plane 1: 270.27 66.00 -10.25
Plane 2: 4.48 80.65 -155.66

Iso.= 5.1% CLVD= 9.5%



05/ 3/ 5 19: 7:58.80

(24.6700, 121.8400)

Depth= 19 km Mw = 5.49

Strike Dip Slip
Plane 1: 358.60 71.27 -170.68
Plane 2: 265.58 81.18 -18.96

Iso.= -2.4% CLVD= 17.7%

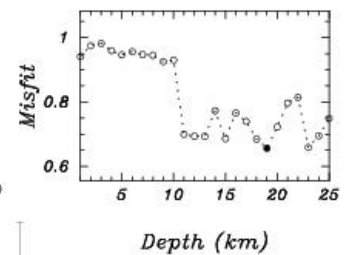
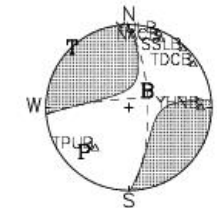


Fig.3. BATS(Broadband Array in Taiwan for Seismology) centroid moment tensor solutions for the first and second mainshocks, 5 March, 2005

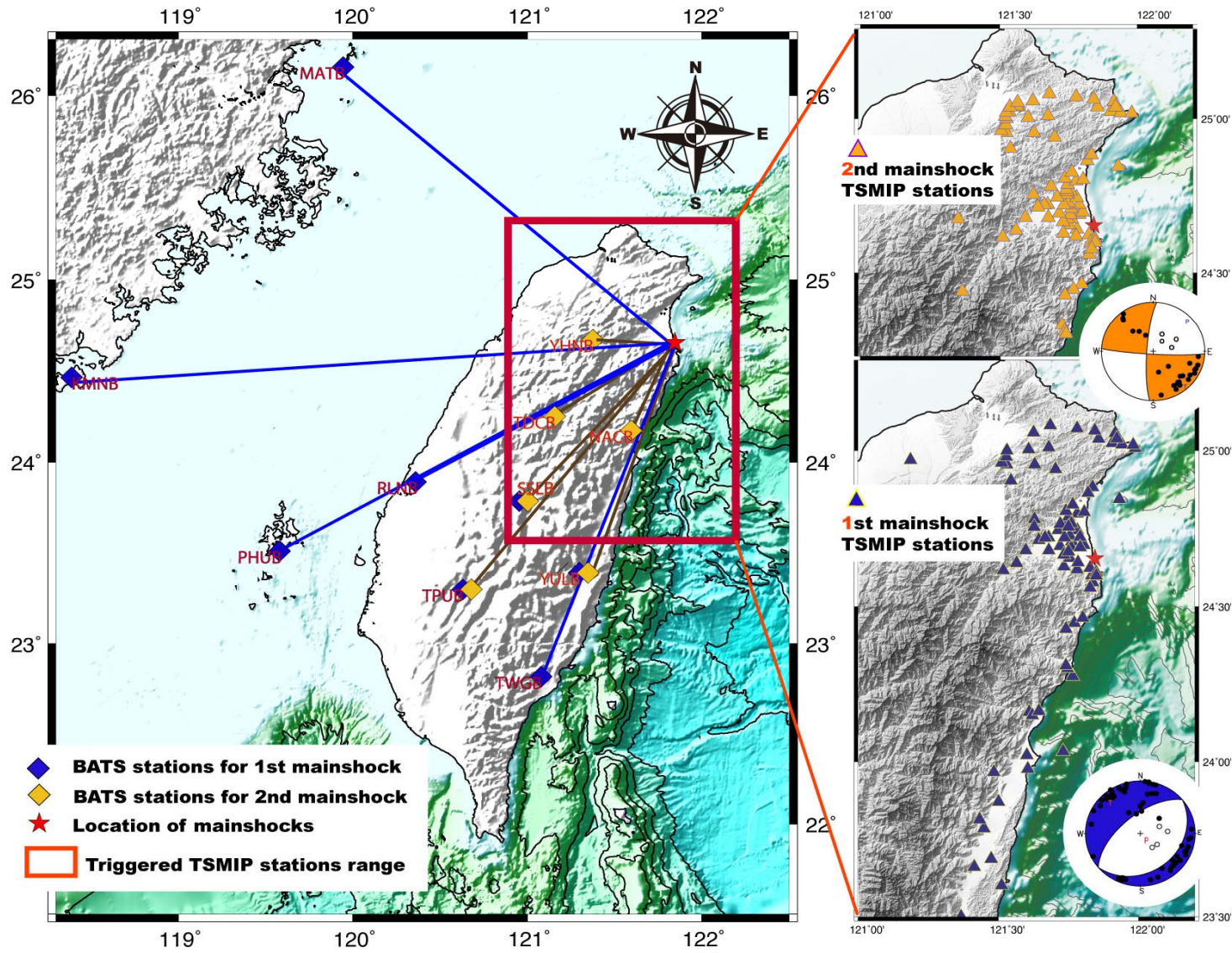


Fig.4 Stations used for centroid moment tensor determination, left panel illustrates BATS stations used in waveform inversion. Right panels are TSMIP triggered stations distribution; the upper corner refers to second mainshock, and the lower to first mainshock.

1.2 Study Strategy and Overview

The strategy and procedure of this study can be described as the following:

1. The work is focused on differentiation between first motion and the CMT inversion method. Basic hypothesis is to be explained initially in theory and then applied on trail tests. In the trail tests, the first mainshock is chosen as the target event, since its distinctness rouses the interest. We use acceleration record of TSMIP array to resolve both first motion solution and moment tensor waveform inversion.
2. Combine with refined one-dimensional velocity structure from modified velocity, and selected well-covering local TSMIP station records, more reliable inversion tests are done to the first mainshock. The calibration for the CMT model parameters are featured in this step.
3. Difference between first motion method and re-calculated inversion result is discussed.
4. Comparing our CMT with BATS CMT results
5. Comparing CMT solution to clustered aftershocks, pinpointed in discussion.

The procedure outlining our study is given below in the flow chart (Fig.5):

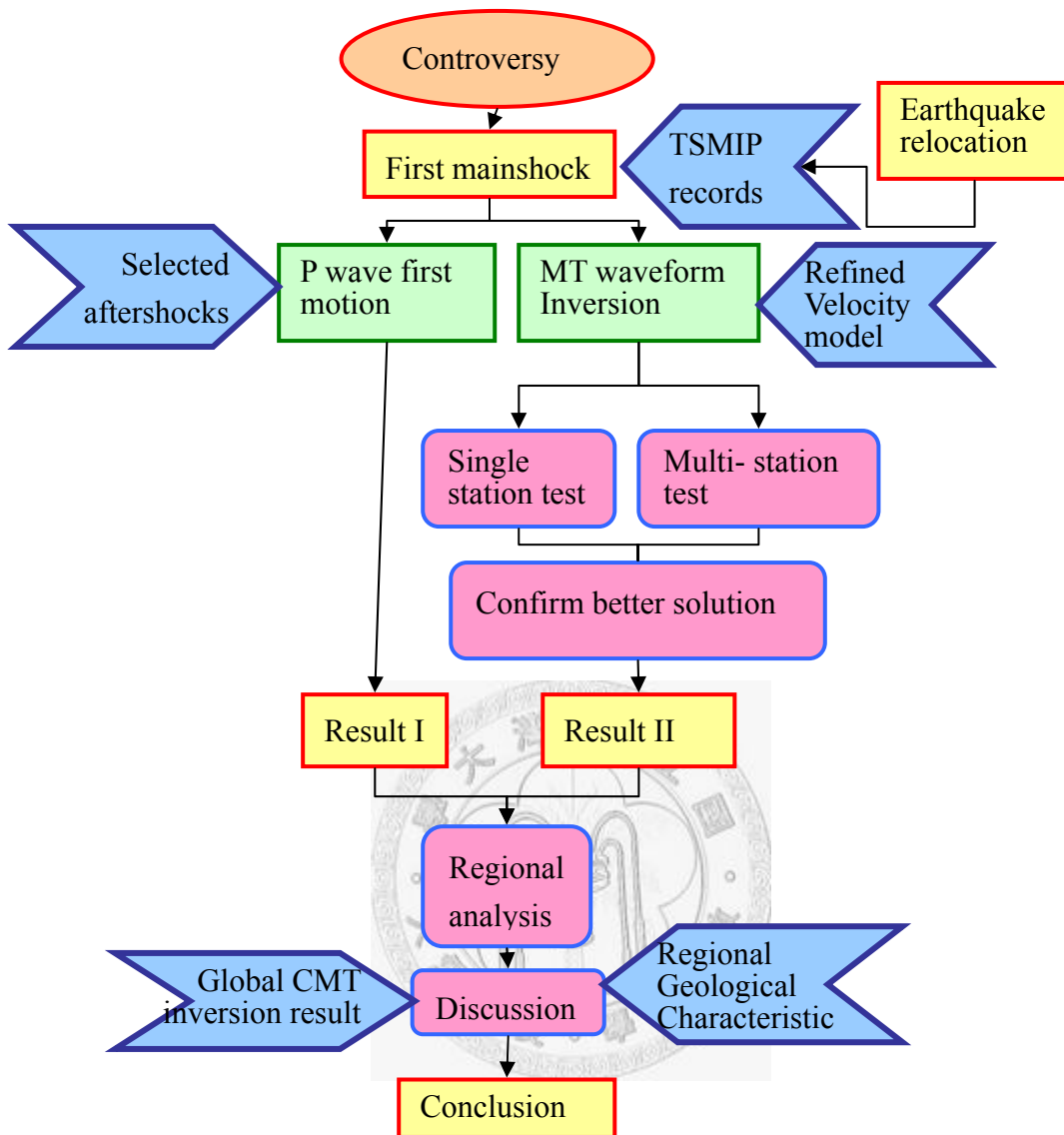


Fig.5 Flow Chart of study procedure.

1.3 Local Geological Background

The Ilan Plain is a triangular-shape flat alluvial plain located at northeastern tip of Taiwan. Its area is around 320 km², with three local towns Sansing, Touchen, and Suao residing at its three tips. According to two previous geological studies (Ho, 1988;

Chiang, 1976) the uppermost layer is modern, unconsolidated, alluvial deposit. Its bedrock is of Miocene age under Pleistocene sediments, adjacent to Oligocene to Miocene shale, hard sandstone or schist in northern extending Hsuehshan range; Also there is early Miocene age hard shale at the southern edge of this isosceles triangle (Fig.6). The eastern side is facing toward the opening of Okinawa Trough and Ryukyu Arc, mostly said as an extrusion between the turning corner of the Phillipine Sea plate subduction with Eurasian and South China Sea plate system (Angelier et. al., 2007). In northeastern Taiwan, Philippine Sea Plate subducts beneath Eurasian Plate dipping northward, and forms upper extension region as Okinawa Trough behind the Ryukyu arc. It is said that from south to north at eastern Taiwan, collision of plate subducting east underneath Phillipine Sea Plate, sutured (Shyu et al., 2005). Base on the focal mechanism analysis by Huang (2006), most of the earthquakes occurred in the Ilan region are normal or strike-slip events.

Most of the structures in northern part of the Ilan plain are parallel in trend of NE-SW. There are two suspicious active faults in this region, Ilan fault and Jiaosi fault reported by Lee et. al. (1998). Other assumptions tended to place previous structures at the joint between Pleistocene sediment and bedrock, which correlates to the geological distinct boundary. The unconformity depth is on average 1500 meters down slightly north of the center of Ilan plain, where Lanyang river lower reach (previously named

Ilan Jhuoshuei river) located. Chiang (1976) proposed six faults, mainly in north portion to the Lanyan river, and one right on lower reach of the river (121.76°-121.82°, 24.78°), which is much closer to recent Ilan earthquake pair location (121.84°E, 24.66°N)(Fig. 7).

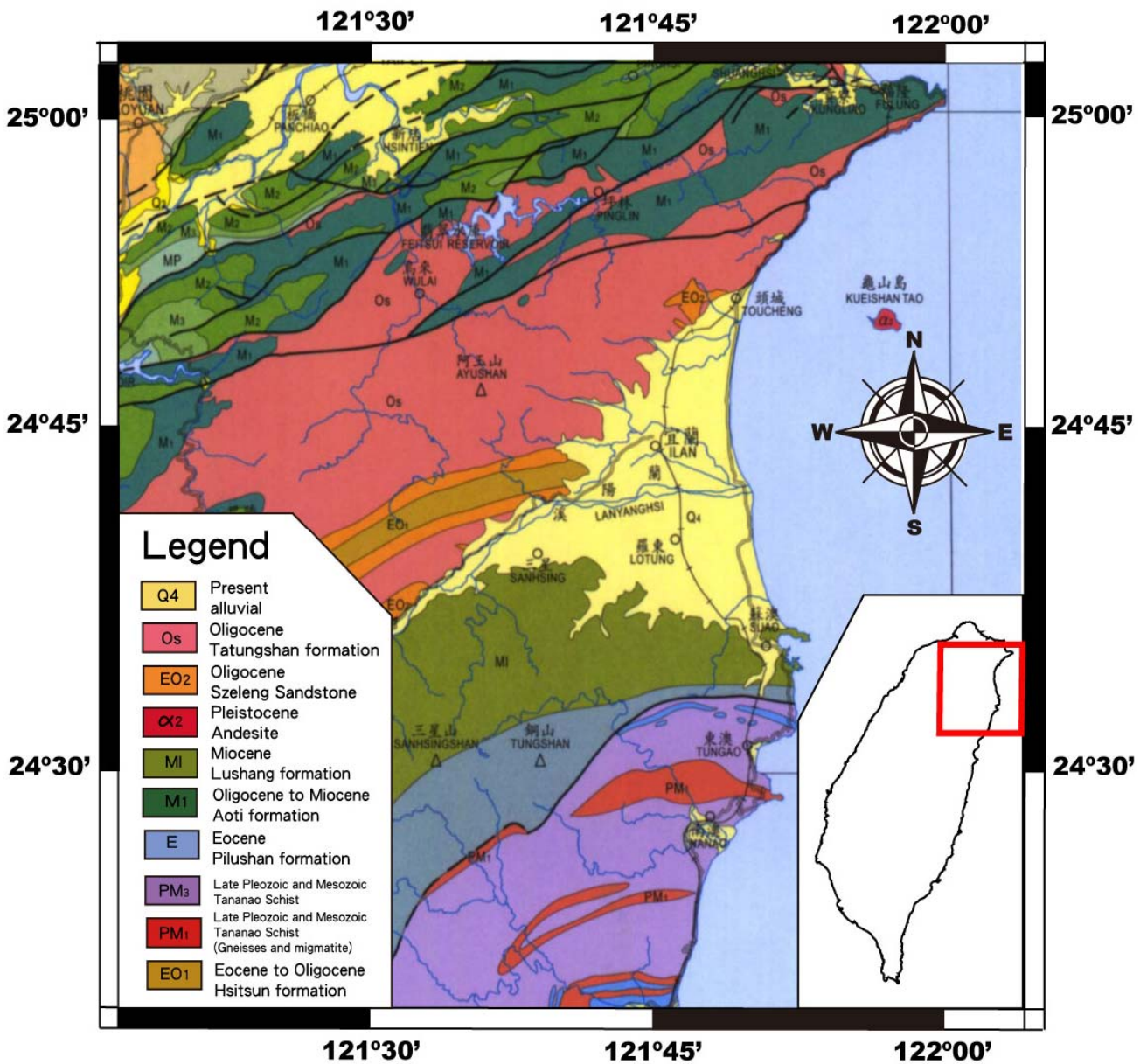


Fig.6 Geological setting of Ilan region, modified from the Geological map of Taiwan. (Central Geological Survey, MOEA, 2000.) For translated terminologies, please refer to Appendix II

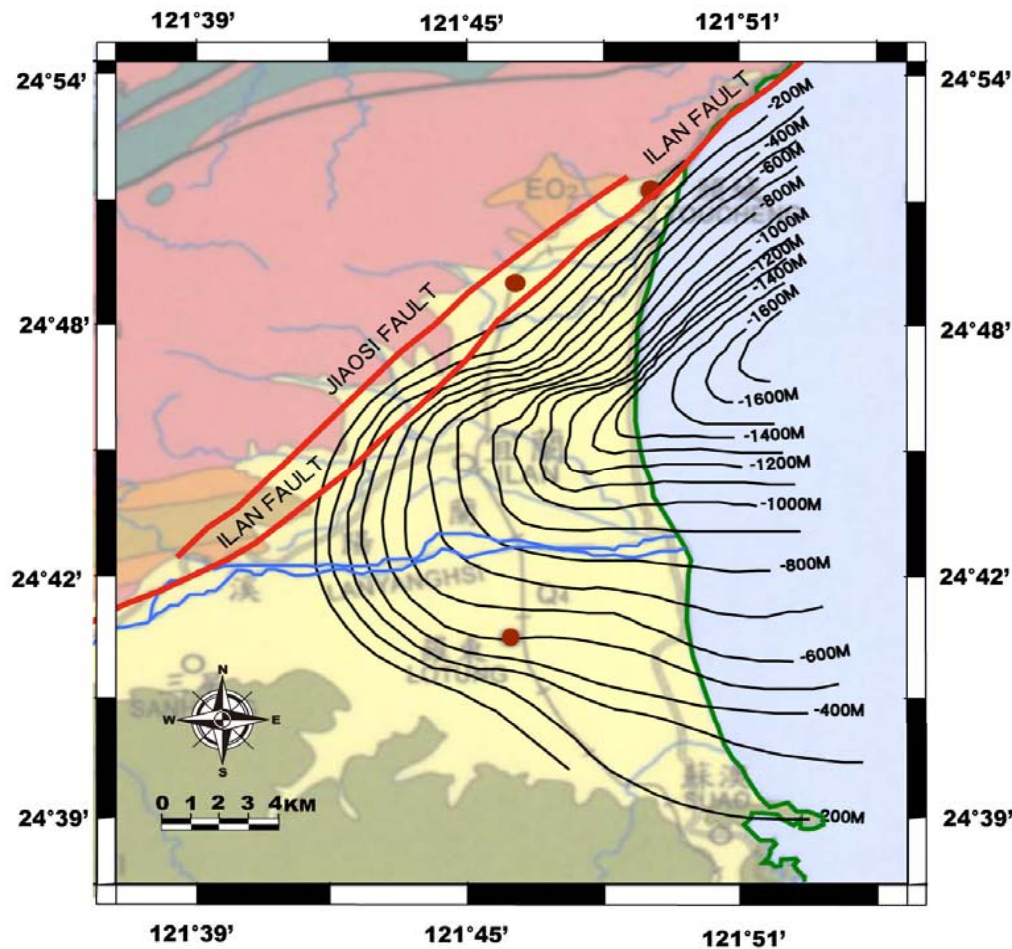


Fig.7 Basement subsurface contour map by Chiang (1976), left panel. Two active faults as the red line were reported by Lee et al. (1998), from right panel, the proposed active faults of Taiwan. Base map modified from Geological map of Taiwan. (Central Geological Survey, MOEA, 2000.) For translated terminologies, please refer to Appendix III.

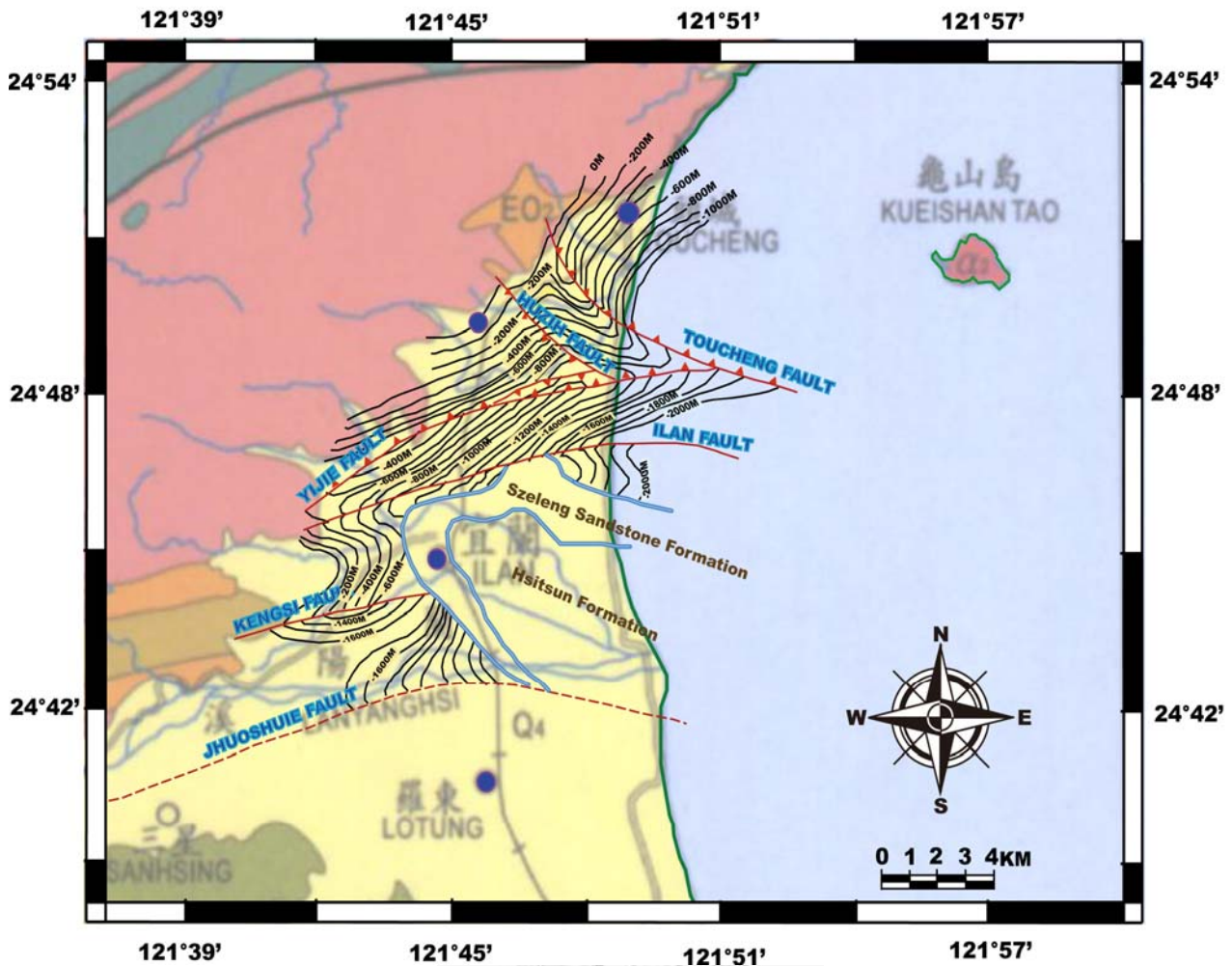


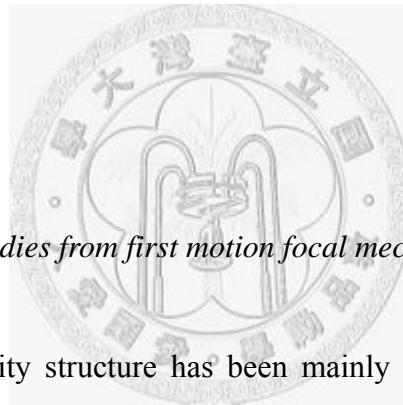
Fig. 8 The fault system constructed from seismic reflection profiles (Chiang, 1976). In comparison with the location of Ilan fault by Lee et al. (1998) in Figure 7, the location of Ilan fault by Chiang(1976) is much closer to Lanyangsi.

1.4 Previous Studies, Comments and Debates

1.4.1 Seismic Reflection

A high-resolution reflection investigation in the Ilan region had been deployed by Chinese Petroleum Company(CPC) in 1973. Totally, eight explosion gallery lines

and reflection profiles were obtained (Chiang, 1976). It is declared to obtain fine recording. There were hand- drawn continuous reflection profiles on gallery lines. And contour map of basement and modern alluvial unconformity were also given in the report (Chiang, 1976; Figure 7 and Figure 8). From this report, the surface weathered soil velocity is given as 500 m/sec, and the most shallow part, modern alluvial deposit, ranges from 1600 to 1800 m/sec. The basement contour is shown in Figure 7. Furthermore, Figure 8 shows the fault system and possible geological structures in NEE direction.



1.4.2 Seismotectonic studies from first motion focal mechanism

Northeastern seismicity structure has been mainly explored for revealing plate motions and pattern of tectonic convergence between two subduction zones, Philippine Sea plate to Eurasia plate at northeastern part and Eurasia plate to Philippine Sea plate at eastern part of Taiwan (Tsai et al., 1977 and Wu, 1978). At the junction of two zones, shallow structure is believed to imply sequential responses. In recent years, studies attempt to accumulate adequate amount of focal mechanisms for local structure interpretation. The technique of first motion focal mechanism is superior on rapid determination. With the increase of stations, better coverage constraint provides better first motion solutions. Thus local dense-arrays can fully support regional studies on

small earthquakes, at smaller scale. Yadav et al.(2004) and Huang et al.(2007) analyzed relocated seismicity around Ilan region and categorized more detail subunits. The earthquake clustering phenomenon is clear in the Ilan region (Figs. 9 and 10).

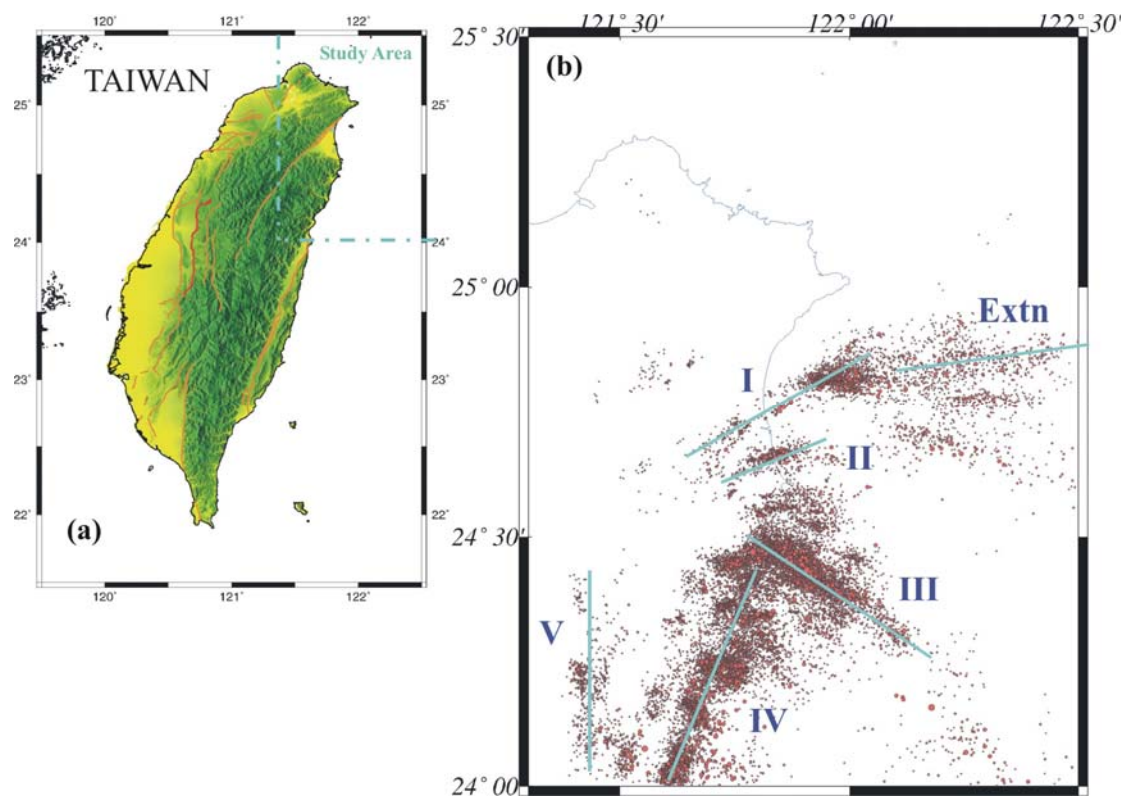


Fig. 9 The shallow seismicity (depth ≤ 30 km) for the Ilan region and clusters classification by Yadav et al. (2004), (a) topographic map of Taiwan and the study region. (b)The distribution of events from 1993-2002, (hypoDD relocated, and first motion focal mechanisms determined by PPFIT). This research divided local seismicity into I~IV subunits. Green lines on right panel are profiles for examining the focal mechanisms in the zone of subunits. The Extn subunit represented extension from the opening of Okinawa Trough, with mostly normal focal mechanisms. From units I to IV, mechanisms turned to be mostly left-lateral strike slip (unit III) or thrust (unit IV and V).

Both Yadav et al. (2004) and Huang et al. (2007) shared the conclusion of a tectonic transition from south to north. Focal mechanisms sequentially turning

northward from thrust, strike-slip, and then normal fault. Normal type mechanisms are direct effect of backarc opening from the Okinawa trough. To the south, a large number of thrust and strike-slip type solutions suggests compression. In between, it is transition zone between back-arc extension and arc-continental collision, with mostly left lateral strike-slip solutions.

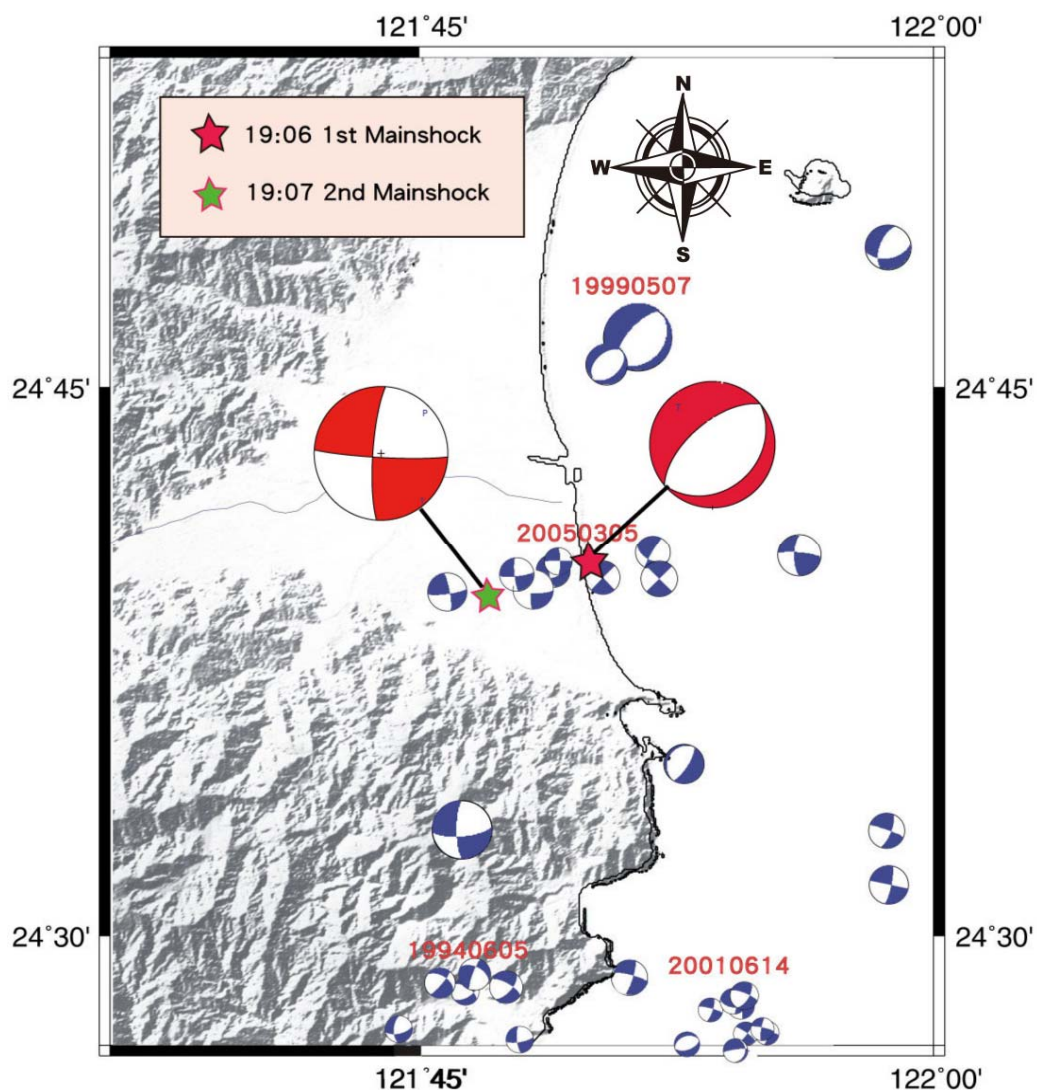


Fig.10 Focal mechanisms distribution of Ilan region determined by Huang et al. (2007) All focal mechanisms were substantiated by the P wave polarities from the Central Weather Bureau Seismographic Network (CWBSN) and TSMIP stations. Blue ones are of regional earthquakes from 2001 to 2005, and the red ones are of 5 March, 2005 mainshocks.

The regional earthquakes had been retrieved from CWBSN catalogue 2001 to 2005 (Fig.10). The clusters were selected with seeds of events over magnitude 5 ($M_L \geq 5.0$) using double linking method. The clustering method linked relevant events only if the event occurred within 3 days time and 5 km range related to firstly the mainshock, and then all related events would be rearranged by time. The latest linked event would be given as new seeds to continue linking process. The clustering would be completed until searching ceased at the time that no further linking was generated. Temporal and spatial thresholds were empirical value successfully tested for the whole-island of Taiwan (Wu and Chiao, 2006; Wu and Chen, 2007). However, in the vicinity region of where the earthquake pair located, there were rare normal records given by first motion method.

1.4.3 Inversion Centroid Moment Tensors

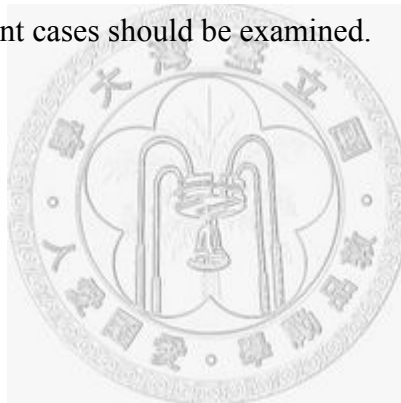
The broadband global network like Harvard (since 1976) and NEID (since 1997) provides mechanisms under assumptions of large scale velocity model. In Taiwan region, Kao et al.(1998b, 1999, and 2002) had provided a series of solutions using BATS CMT solutions. For the northeastern region, they indicated lateral compression seismic zone between downdip extension in north and collision in south (Kao et al.,

1998b). Liang et al. (2005) further analyzed several earthquake clusters using BATS solutions. They proposed left lateral strike slip at where 2002/05/15 and 2005/03/05 earthquake series located. These are considered correlating to the boundary of sharp geological units, and the tip of Okinawa Opening.

Observation of Liang et al. (2005) brought up much attention to 5 March, 2005 earthquake pair. The most doubted problem is that two earthquakes occurred in a close time (1.08 minutes). For distanced-station records as BATS, waveform of the first event would be contaminated by the second one. Tsao (2006) also addressed this difficulty in his study. They used different method but also the near-field TSMIP local records to avoid such problem.

Inversion mechanisms can be used more precisely to interpret earthquake source. It is after generalized ray theory that point source can be applied to hypothesize single phases (Helmberger, 1974, Gilbert and Helmberger, 1972, and Langston and Helmberger, 1975). Basic computation methods used to generate complete solutions to synthetic waveforms are discrete wavenumber/finite element (Olson and Aspel, 1982), finite-difference method (Alekseev and Mikhailenko, 1980), wave integration method (Herrmann, 1979; Wang and Herrmann, 1980), and discrete wavenumber method (Bouchon, 1981). Discrete wavenumber method is widely accepted for its computing simplification. Rather, the wave integration method provides a more realistic approach

for complication at authentic ray path. We adopted the wave integration method in consideration of the local structure. Huang (1994) tested the kernel waveform integration method adopted from R. B. Herrmann (1985). With the verification of record from Chengkung earthquake (23.15N, 121.35E; ML=5.4; depth 13.7 km), he claimed that single station CHK (23.10N, 121.37E) is applicable to obtain appropriate inversion moment tensor. Such short-distance records and empirical application for point source approximation were rare. More tests are needed for different region of Taiwan, and the proper application to different cases should be examined.



2. Method and Theory

2.1 First Motion Focal Mechanism Determination

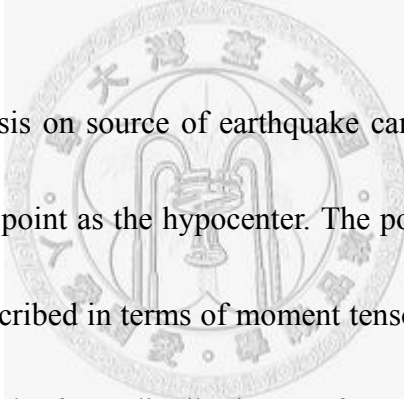
The focal mechanisms were determined from both the regional TSMIP and CWBSN recordings. These data contain P and S wave polarities including the up or down-going direction of first arrival P wave (vertical), azimuth, epicenter distance and delay time comparing to theoretical values. These data mainly assume wave transferring and arrival time according to the view of ray theory. All records were relocated with previous 3D velocity model from Wu et al. (2007).

The fault-plane strike, dip, and also rake directions are manually calibrated to generate stereographic projection to the lower hemisphere. Then it is compared with upward and downward observation records in vertical data to check for fitness. It is chosen to be the best solution that station coverage is fully dispersing to the whole hemisphere (more than three quadrants of focal mechanism is divided by at least one data point). Re-examination is done by checking possible angle shifts of the plane. There were three ranks to classify the quality of focal mechanism determined by this method. The top rank still suits the data distribution within 10~15 degrees, with four quadrants of station coverage; i.e. Fig.1). Noticeably, in the case of CWB data used for

first motion determination, the upward going ray paths received are rotated 180° in station azimuth to project to the lower hemisphere. This procedure confirms the right distribution to be projected on physical assumption of theorized ray path. Some more examples are examined in Chapter 4 (Fig.) if further confirmation needed.

2.2 Moment Tensor Solution –Theory

2.2.1 Hypothesis



Basic physical hypothesis on source of earthquake can be attributed to equivalent body force pairs at a single point as the hypocenter. The point source activated with an energy release, which is described in terms of moment tensors in matrix form (2-2-1-6). With directions involved in the force distribution, surface displacement can be attained through frequency domain integration of the effects from source to receiver. Frequency band can be chosen according to approximation demand, and well finalized to compare with filtered observation. Also, taken band should be in the range of the seismometer response to avoid source information lost. Formulation by using seismic sources representation (Aki and Richards, 1980; Jost and Herrmann, 1989), observed displacement d_n at an arbitrary position \mathbf{x} at time \mathbf{t} , due to a distribution of equivalent body force densities f_k , in a source region is :

$$d_n(x,t) = \int_{-\infty}^{\infty} \int_V G_{nk}(x,t,r,\bar{t}) f_k(r,\bar{t}) dV(r) d\bar{t} \quad (2-2-1-1)$$

where G_{nk} is Green function containing propagation effect with imposed velocity media, V the source volume in which f_k is non-zero. Hence, through proper and modest adjustments on position, Green function around new reference point is :

$$G_{nk}(x,t,r,\bar{t}) = \sum_{m=0}^{\infty} \frac{1}{m!} (r_{j_1} - \xi_{j_1}) \cdot (r_{j_2} - \xi_{j_2}) \cdots (r_{j_m} - \xi_{j_m}) G_{nk,j_1 \dots j_m}(x,t,\xi,\bar{t}) \quad (2-2-1-2)$$

The expansion is done around $\mathbf{r} = \xi$ (all vectors in space), where physical source is represented by existence of equivalent forces. Original time dependent force moment tensor is defined as:

$$M_{kj_1 \dots j_m}(\xi,\bar{t}) = \int_V (r_{j_1} - \xi_{j_1}) (r_{j_2} - \xi_{j_2}) \cdots (r_{j_m} - \xi_{j_m}) f_k(r,\bar{t}) dV \quad (2-2-1-3)$$

Jointing expansion (2-2-1-2) and (2-2-1-3), displacement can be written as terms resolving details by source M_k and path G_{nk} effects:

$$d_n(x,t) = G_{nk,j}(x,t,\xi,\bar{t}) * M_{kj}(\xi,\bar{t}) \quad (2-2-1-4)$$

The notation * indicates temporal convolution. Once a generalized assumption is made that every time-dependent seismic moment tensors have equivalent time function-- $s(\bar{t})$ (Silver and Jordan, 1982), (2-2-1-4) can be simplified as :

$$d_n(x,t) = M_{kj} [G_{nk,j} * s(\bar{t})] \quad (2-2-1-5)$$

The time function, which shape can be determined differently by preferences, is assumed to conform to formulation (2-2-1-5), the moment tensor value is then split out to be fixed according to specific source effect, simply as in (2-2-1-6).

$$\begin{bmatrix} M_{xx} & M_{xy} & M_{xz} \\ M_{yx} & M_{yy} & M_{yz} \\ M_{zx} & M_{zy} & M_{zz} \end{bmatrix} \quad (2-2-1-6)$$

All these tensors representing the equivalent forces at a confined volume, are greatly illustrative under adequate control over modest receiver distances, and the wavelength of selected frequency band in comparison to fault dimension. We can also illustrate (2-2-1-6) transferring to fault plane coordinates set on the plane (2-2-1-7), and also, coordinates commonly used in geology (2-2-1-8):

$$M_{kj} = \mu A (u_k v_j + u_j v_k) \quad (2-2-1-7)$$

the vector \mathbf{u} denotes the slip on fault surface (two dimensional), and vector \mathbf{v} denotes the vector normal to fault plane, which indicates direction of fault plane in the space (Aki and Richards, 1980; Jost and Herrmann, 1989).

$$\begin{aligned} M_{xx} &= -M_0 (\sin \delta \cos \lambda \sin 2\Phi + \sin 2\delta \sin \lambda \sin^2 \Phi) \\ M_{yy} &= M_0 (\sin \delta \cos \lambda \sin 2\Phi - \sin 2\delta \sin \lambda \cos^2 \Phi) \\ M_{zz} &= M_0 (\sin 2\delta \sin \lambda) \\ M_{xy} &= M_0 (\sin \delta \cos \lambda \sin 2\Phi + 0.5 \sin 2\delta \sin \lambda \sin 2\Phi) \\ M_{xz} &= -M_0 (\cos \delta \cos \lambda \cos \Phi + \cos 2\delta \sin \lambda \sin \Phi) \\ M_{yz} &= -M_0 (\cos \delta \cos \lambda \sin \Phi - \cos 2\delta \sin \lambda \cos \Phi) \end{aligned} \quad (2-2-1-8)$$

The x, y and z is under coordinate set arbitrarily in the space. As the geological recording, δ , λ and Φ signify the dip, slip and strike of the fault as reference to horizontal down, counterclockwise from horizontal and clockwise from north. The moment tensors is made symmetric from upper-triangle portion of matrix form (2-2-1-6), for the reason that double couple force at M_{kj} (where $k \neq j$) elements are

indiscriminative to the proposed fault plane and auxiliary plane. In the sense of equivalent force, two pairs of orthogonal planes basically demonstrate an equivalent case.

2.2.2 Green's Function and Synthetic

As we stated in formulation (2-2-1-5), Green's function stands for path effect with a point source triggering, usually an impulse. Without taking into account of the rupture directed information – the moments M_{kj} , Wang and Herrmann (1980) presented the Fourier-transformed displacement at the free surface at a distance r from the origin point source

$$\begin{aligned}
 u_z(r,0,\omega) &= ZSS[(f_1n_1 - f_2n_2)\cos 2\Phi + (f_1n_2 + f_2n_1)\sin 2\Phi] \\
 &+ ZDS[(f_1n_3 + f_3n_1)\cos \Phi + (f_2n_3 + f_3n_2)\sin \Phi] \\
 &+ ZDD[f_3n_3] \\
 u_r(r,0,\omega) &= RSS[(f_1n_1 - f_2n_2)\cos 2\Phi + (f_1n_2 + f_2n_1)\sin 2\Phi] \\
 &+ RDS[(f_1n_3 + f_3n_1)\cos \Phi + (f_2n_3 + f_3n_2)\sin \Phi] \\
 &+ RDD[f_3n_3] \\
 u_\phi(r,0,\omega) &= TSS[(f_1n_1 - f_2n_2)\sin 2\Phi - (f_1n_2 + f_2n_1)\cos 2\Phi] \\
 &+ TDS[(f_1n_3 + f_3n_1)\sin \Phi - (f_2n_3 + f_3n_2)\cos \Phi]
 \end{aligned} \tag{2-2-2-1}$$

The representations in capital letters are abbreviations generalized from the concept of point source wave radiation pattern. The formulation is oriented to fault strike, dip, and slip -- Φ_f , δ_f and λ_f . And the synthesized displacements, here with symbol \mathbf{u} , in frequency domain, are under cylindrical coordinates setting with \mathbf{r} the radius, Φ the

strike and z the hypocenter depth. Some more deductions about indexes in (2-2-2-1) are given below (2-2-2-2). It is in arrangement from Haskell, 1964, Jost and Herrmann, 1989, Herrmann and Wang, 1985, and, overview of CPS version 3.3.0 by Herrmann, 2002. Please refer to above-mentioned papers for details.

$$\begin{aligned}
 f_1 &= \cos \lambda_f \cos \Phi_f + \sin \lambda_f \cos \delta_f \sin \Phi_f \\
 f_2 &= \cos \lambda_f \sin \Phi_f - \sin \lambda_f \cos \delta_f \cos \Phi_f \\
 f_3 &= -\sin \lambda_f \sin \delta_f \\
 n_1 &= -\sin \Phi_f \sin \delta_f \\
 n_2 &= \cos \Phi_f \sin \delta_f \\
 n_3 &= -\cos \delta_f
 \end{aligned}
 \tag{2-2-2-2}$$

In the (2-2-2-2), there is the force direction and fault normal vector in reference to any kind of proposed fault plane.

Position	Green's Function	Description	
1	ZDD	Vertical Component	45° dip slip
2	RDD	Radial Component	45° dip slip
3	ZDS	Vertical Component	90° dip slip
4	RDS	Radial Component	90° dip slip
5	TDS	Tangential Component	90° dip slip
6	ZSS	Vertical Component	vertical strike-slip
7	RSS	Radial Component	vertical strike-slip
8	TSS	Tangential Component	vertical strike-slip

Fault type representations adopted from Herrmann (2002).

Herrmann and Wang, (1985), summarize the Green's Function indexes more thoroughly.

Integration done in discrete frequencies ω helps us construct synthetic displacement

waveform, regarding path effect to of one impulse point source, or composed with source moments like double-couple, isotropic, or Compensated linear vector dipole (CLVD) components for advance.

2.2.3 Inversion

We use mainly SVD (Singular Value Decomposition) solution inversion method to retrieve moment tensors. The SVD computation subroutine is adopted from Numerical Recipe in Fortran, 2th edition. Comparison between observation data and synthetic is done by Chi-square statistics, formula given below:

$$\chi^2 = \sum \left(\frac{d - G \cdot M}{\sigma} \right)^2 \quad (2-2-3-1)$$

The χ^2 is Chi-square index, d represents the observed waveform data, $G \cdot M$ as the predicted synthetic data calculated from local Green function, and σ , the standard deviation, which is assigned as 1.0 in this study. The program used in this study calculated a solution for a moment solution which minimizes Chi-square index. Under the constraint of observed waveform \mathbf{d} , simple inversion relation re-write from (2-2-1-5) :

$$\mathbf{u}_{obs} = \mathbf{G}_{syn} * \mathbf{M} \quad (2-2-3-2)$$

The difference here is that displacement \mathbf{d} changes to be observed data \mathbf{u}_{obs} , and \mathbf{G}_{syn} indicates the Green functions derived in last section purely with assumptions of velocity

model, time function set, and physical spreading method used. \mathbf{M} , be the moment tensor representing the finite fault we wish to know. Generally, the inverse problem is solved to minimize squared difference between synthetic and observation (the L2 norm) , and we can describe SVD method as following (Menke, 1989):

$$\text{The inverse equation: } \mathbf{u} = \mathbf{G}\mathbf{M} \quad (2-2-3-2)$$

Where Matrix \mathbf{G} can be constructed as :

$$\mathbf{G} = \mathbf{U}\mathbf{\Lambda}\mathbf{V}^T \quad (2-2-3-3)$$

in which, Matrix \mathbf{G} has portion G_p that lies in the space helpful to resolve model, or, the parameters span by data space (supported by data). G_0 lies in the space indiscriminative from the data to resolve model (not supported by data). In other words, the existence of G_0 has no effects on resolving model.

$$\mathbf{G} = \begin{bmatrix} G_p & 0 \\ 0 & G_0 \end{bmatrix} = \begin{bmatrix} U_p & U_0 \end{bmatrix} \begin{bmatrix} \Lambda_p & 0 \\ 0 & 0 \end{bmatrix} \begin{bmatrix} V_p \\ V_0 \end{bmatrix} \quad (2-2-3-4)$$

\mathbf{U} , the data dimension, and \mathbf{V} , the model dimension, are also decomposed into p and 0 space. Therefore, we can disregard 0 space since it is not helpful in model resolution.

$$\mathbf{G} = U_p \Lambda_p V_p^T \quad (2-2-3-5)$$

Thus, take (2-2-3-5) into (2-2-3-2) and rearranged :

$$\begin{aligned} U_p \Lambda_p V_p^T \mathbf{M} &= \mathbf{u} \\ \Lambda_p (V_p^T \mathbf{M}) &= U_p^T \mathbf{u} \end{aligned} \quad (2-2-3-6)$$

New inversion formulation exchanges \mathbf{M} with the effective model matrix $V_p^T \mathbf{M}$, and \mathbf{u}

with the effective data space $U_p^T u$. In addition, it is convenient to deal with the diagonalizable Λ_p to solve the model.

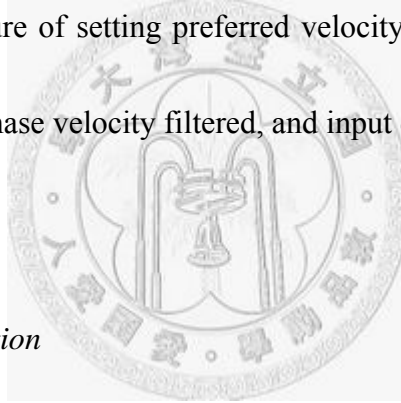
$$\begin{aligned} V_p^T M &= \Lambda_p^{-1} U_p^T u \\ \widehat{M} &= (V_p \Lambda_p^{-1} U_p^T) u \end{aligned} \quad (2-2-3-7)$$

The predicted model is determined once we find V_p , U_p and Λ_p in the original \mathbf{G} , by inverse, transpose, and multiply all that mentioned above. This method is a powerful tool to retrieve inversion problem while model parameter number is less than 1000. For further surpass, calculation would be overloaded. We access moment tensor model from observed displacement data with SVD method first. Then we use this moment tensor solution as an input to get synthetic seismograms by what stated in (2-2-1-5). Procedure like this forms the basic one-way direction for solution. After the inversion procedure, theoretically there should be perfect symmetrical moment tensor components and no net force on diagonal terms at the tensor matrix. A tensor like this represents pure shearing or slip for a simple shallow fault without volume change. However, sources within the earth can sometimes have net force and torque components, described by first-rank and asymmetric second-rank moment tensors. These non-double couple components are well attributed to the dilation or compression term—the compensated linear vector dipole (CLVD) percentage. The lower the CLVD, the more plausible that we believe it's a standard shear-pattern earthquake. It is preferred to minimize CLVD to the lowest in our study for initial understanding of the case.

2.3 Synthetic Seismogram Computation

2.3.1 Wave Integration

In this study, computation of synthetic seismograms adopts the idea of wave integration method (Herrmann, 1979; Wang and Herrmann, 1980). The values of $u_r(r, \Phi, 0, \omega)$, $u_\phi(r, \Phi, 0, \omega)$, and $u_z(r, \Phi, 0, \omega)$ are calculated at several discrete frequencies in the range of interest. We had our synthetic waveform computation calculated with the procedure of setting preferred velocity model, giving fixed source depth and receiver depth, phase velocity filtered, and input distance file for each station.



2.3.2 Source Time Function

The time function assumed (2-2-1-5) should be formerly set in program, converted by Fourier transform and composed to Green's function. Usually, time function captures the characteristic of an impulse release at time series, in which triangle and parabolic are both probable. In this study we use parabolic pulse after Herrmann, 1979 :

$$s(t) = \begin{cases} 0 & t \leq 0 \\ 0.5 \times \left(\frac{t}{\tau}\right)^2 & 0 \leq t \leq \tau \\ -0.5 \times \left(\frac{t}{\tau}\right)^2 + 2 \times \left(\frac{t}{\tau}\right) - 1 & \tau \leq t \leq 3\tau \\ 0.5 \times \left(\frac{t}{\tau}\right)^2 - 4 \times \left(\frac{t}{\tau}\right) - 8 & 3\tau \leq t \leq 4\tau \\ 0 & t \leq 4\tau \end{cases} \quad \text{for} \quad (2-3-1)$$

τ is one forth the given pulse duration in considering rise time on a single point. It is set that $\tau=0.2$ for all inversion in our study for an adequate rupture duration for a magnitude 5.9 event. Shape of parabola is given below (Fig.9). Rise time duration and amplitude are all normalized to 1 for unit area purpose.

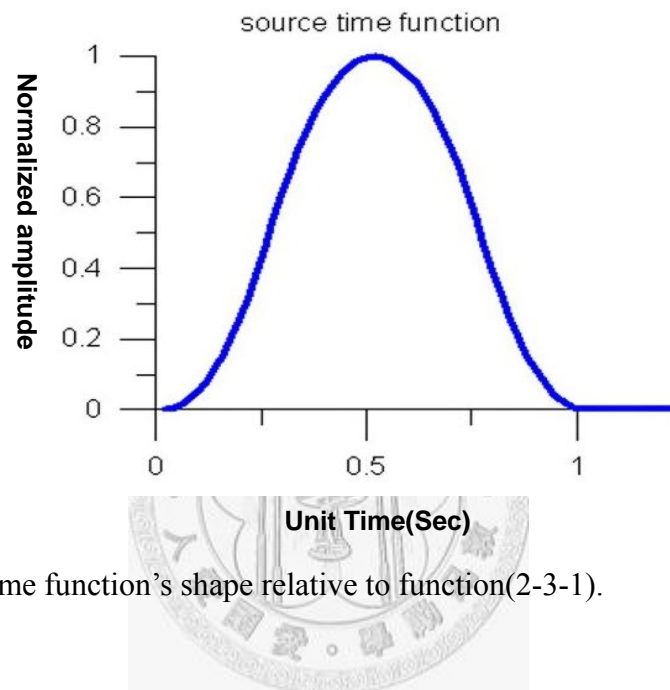


Fig .11 Source time function's shape relative to function(2-3-1).

2.3.3 Phase

All phases considered in our study focus on the range of phase velocity from 1.5 to 8.5 km/s (apparent velocity). From one point of view, it is more information involved when more seismic phases are contained in waveform fitting. In the other, modeling too much phases complicates the inversion procedure and makes the result unstable. Body waves including P and S wave with traveling velocity around 2.0~ 9.0 km/s for general range from surface to 50 km depth are set in our velocity model. The program

automatically involves all phases calculated from theory which is up-going or down-going waves. Considering these body waves and conversion waves as P-SV or SH-P phases, the apparent velocity filtering is adequate for cases of a near field event simulation like this study.

2.4 Wave Integration and Correction

The waveform is displacement integrated from acceleration. It is noted by Boore (2001) that a double integration of the acceleration data often leads to unreasonable results, and baseline corrections are therefore required in most cases before the integration step. Between two-step integration of the TSMIP acceleration, we removed the total trend from the waveform as the demean procedure. It is a simplified procedure to treat the baseline drift phenomenon. And the demean procedure would cancel such defects in the whole sector of waveform selected.

2.5 Single Station Approach

The TSMIP stations offer a good coverage of this event. Firstly, the records from TSMIP is used for moment tensor inversion with single station approach (Huang, 1994). For a primitive simple model test on velocity, we take half-space whole layer

model with P wave velocity 5.381 km/s and S wave velocity 2.984 km/s in trail test. We focus on the first mainshock to concentrate on the controversy between normal and strike-slip component of this event. The waveform filter band on frequency is given in 0.3 ~0.5 Hz, and this is considered a proper but rather high frequency band. For most near-field inversion, the filter band is generally between as low as 0.01 to as high as 2 for different phases. Twenty three station records are taken for single-station test, and each solution expresses identically the mainshock at 19:06. Waveforms are fitted between chosen 12 seconds of synthetic and observation. Since most of TSMIP stations do not equip a unit time base, the P arrival from observed and synthetic waveforms are line up as the reference time. Drastic pre-assumptions on this first mainshock moment tensor inversion are: (1) half-space velocity model, and (2) to fit single station record. Therefore this is called single station approach.

2.6 Multi-station Approach

A better solution to one, and local event will be refined if we adjust to the following: (1) more precise velocity structure, and (2) combined records from multi-stations. A modified velocity structure to suit regional considerations would alleviate the over generalization on velocity and serve for a chance to raise frequency range on fitting local near-field records. Involving more information would cancel out

variations from each path and lateral velocity anomalies to each site. It is expected that to scarify on waveform fitting would help concentrate on approaching the true averaged moment tensor solution from combined station records.

In consideration of its coverage in station distribution, 15 stations' records are taken across Lan-yang river (Fig. 18). Parameters of stations selected can be referred to Table 3, the green shaded rows as used in this approach. We further calculate green function based on averaged tomography result as mentioned in Chapter 3.3. Fitting frequency on waveform decreases down to 0.1~0.3 Hz for the appropriate range, but this range is still high enough to obtain the averaged slip from this case. Earthquake hypocenter is set fixed horizontally after relocation correction. Several repeated trails changing the focal depth will be helpful to probe its effects to misfit and CLVD percentage.

3. Data and Material

3.1 Central Weather Bureau Seismic Network (CWBSN) Earthquake

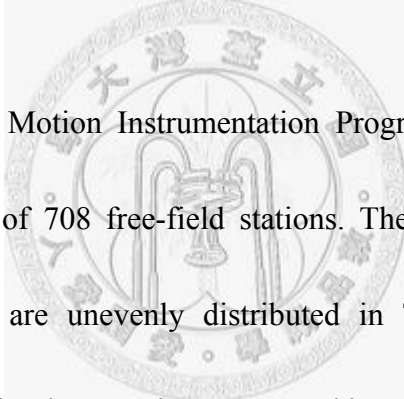
Catalogue

The CWBSN station record used in this study facilitated fundamental records to determine first motion focal mechanisms. The P and S arrivals and P wave polarities from the CWBSN were used in this study to determine hypocenters and focal mechanisms, respectively. The relocation process includes the station records of CWBSN. The Seismological Observation Center of the Central Weather Bureau (CWBSOC) was established at 1989, by expanding the original seismological network with the implementation of 31 three-component seismometers, while maintaining the previous 19 stations. All the stations have facilitated the enhanced coverage of network in Taiwan. At 1991, the Taiwan Telemetered Seismograph Network (TTSN), previously functioning under Institute of Earth Sciences (IES), and Chianan local network owned by Nation Chung Cheng University (NCCU) was combined into original Central Weather Bureau (CWB) network. The complete network with such high density is called Central Weather Bureau Seismic Network (CWBSN), operated by Central Weather Bureau Seismology Center (CWBSOC). Since 2003, there are 94 real-time

stations, 70 of them implemented with S13 type velocity seismometers, which is highly sensitive. There are 86 stations equipped with the A900A type accelerometers for earthquake rapid reporting and early warning purposes (Wu et al., 1997, 1998, 1999, 2007; Wu and Teng, 2002).

3.2 Taiwan Strong Motion Instrumentation Program (TSMIP) Strong

Motion Station



The Taiwan Strong Motion Instrumentation Program (TSMIP) accelerometer network currently consists of 708 free-field stations. The locations are shown as in Figure 12. These stations are unevenly distributed in Taiwan Island in space of approximately 5 km. These implementations are started in August 1992, and the majority start operation by December 1994, belonging to Central Weather Bureau (CWB). CWBSC completed the installation of 570 sites in 1992, 1993 and 1994 with respect to time. By June 1997, all stations had been deployed. Each operating free-field station is equipped with tri-axial accelerometers, digital recording sub-unit, power supply and a timing system.

The main purpose of TSMIP net is to record larger earthquake ($M_L \geq 4.0$) and provide rapid location, magnitude, and intensity record for warning system. This design

has enhanced our ability to monitor larger earthquakes and furthermore helped on collection of high-quality recordings of near-field, and wide frequency resolution band. For such purpose, stations are designed to deploy densely at where capable (Fig.12). Classification of sites are referred to Lee et al.(2001).

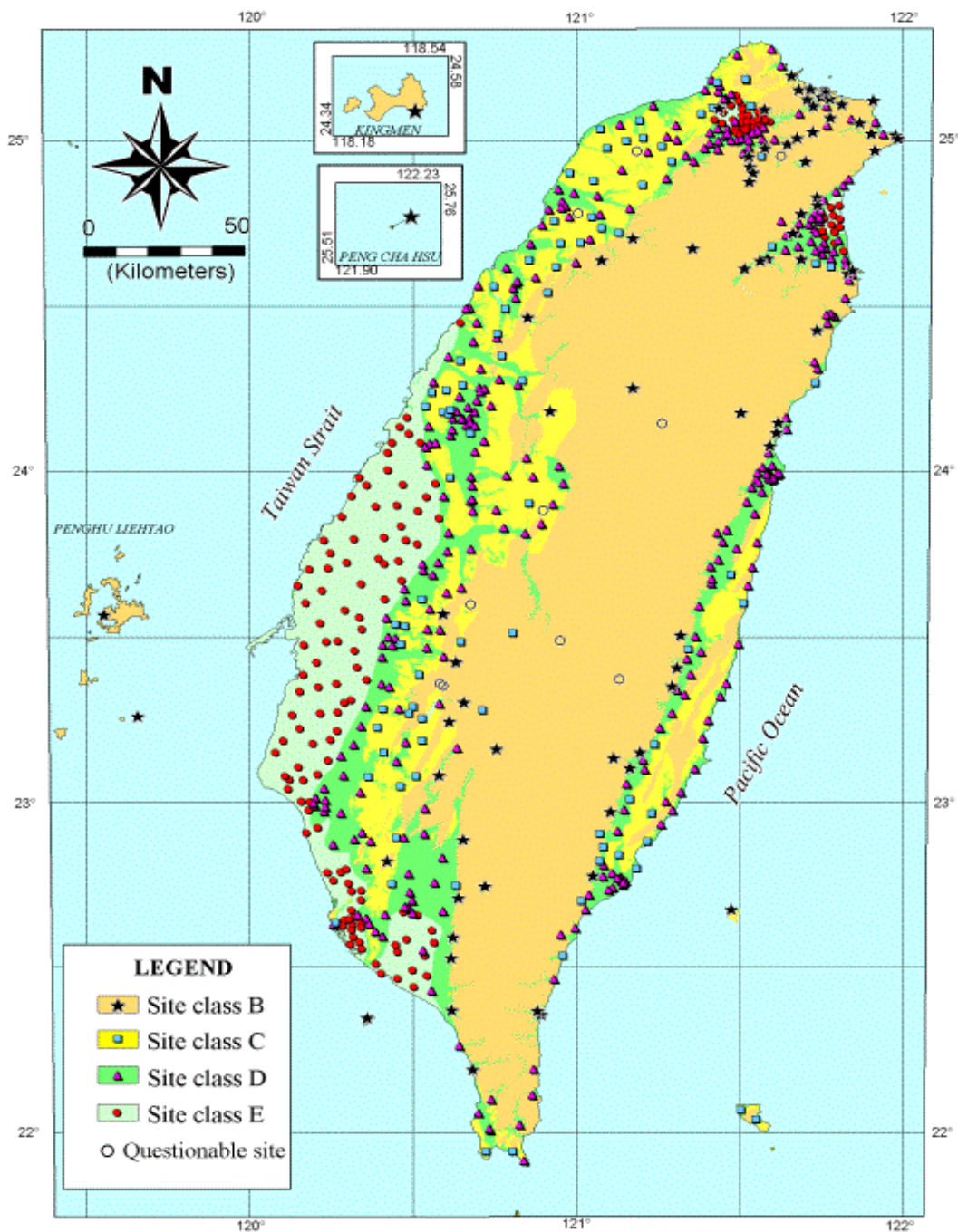
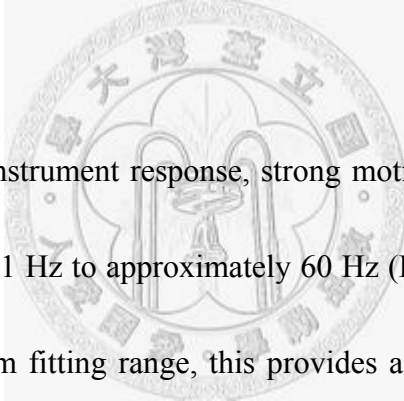


Fig.11 TSMIP stations and site classifications(Lee et al., 2001).

Station sites selection is set as following (Lee, 2001):

1. In nine major metropolitan areas, including TAP(Taipei), HSN(Hsinchu), TCU(Taichung), CHY(Chiayi), TAI(Tainan), KAU(Kaoshiung), ILA(Ilan), HWA(Hwalien) and TTN(Taitung).
2. Near known fault zones.
3. At geological sites of different characters: rock, soil and medium-stiff soil.
4. Near important construction, industrial sites or nuclear power plants.



With regard to instrument response, strong motion accelerometers have full resolution to energy from 0.1 Hz to approximately 60 Hz (Fig.13, Liu, 1999). Thus, for various choices in waveform fitting range, this provides a flexible frequency range to choose from for our study. The TSMIP instrument model contains type of A800, A900, A900A, IDS and SSA. Components, polarity and other data format please refer to Appendix II. Maximum accelerograph amplitude is up to ± 2 g. Each record contains 16-bit high resolution, with sampling rate as high as 200 bps.

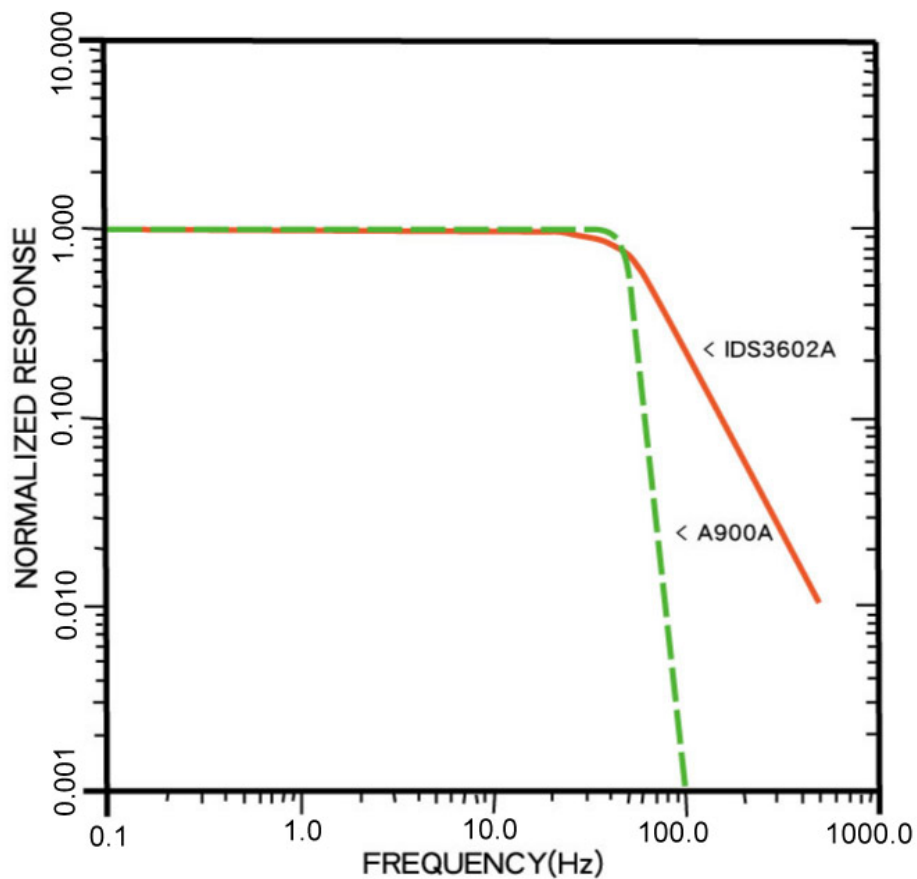


Fig.12 TSMIP instrument response curve in relation to frequency (Liu et al., 1999).

In convenience of the dense distribution of stations on the Ilan plain (Fig.14), we can obtain more detail of Ilan regional earthquakes using the data set from TSMIP. Fortunately, the Ilan area has 69 stations in code of ILA, 5 in code of TRB implemented. There are in total 251 TSMIP stations recorded the 5 March 2005 first mainshock, and 198 stations out of the selected Ilan area. Fine records are selected out from these regional data to obtain our inversion and surface displacement result (Fig.14).

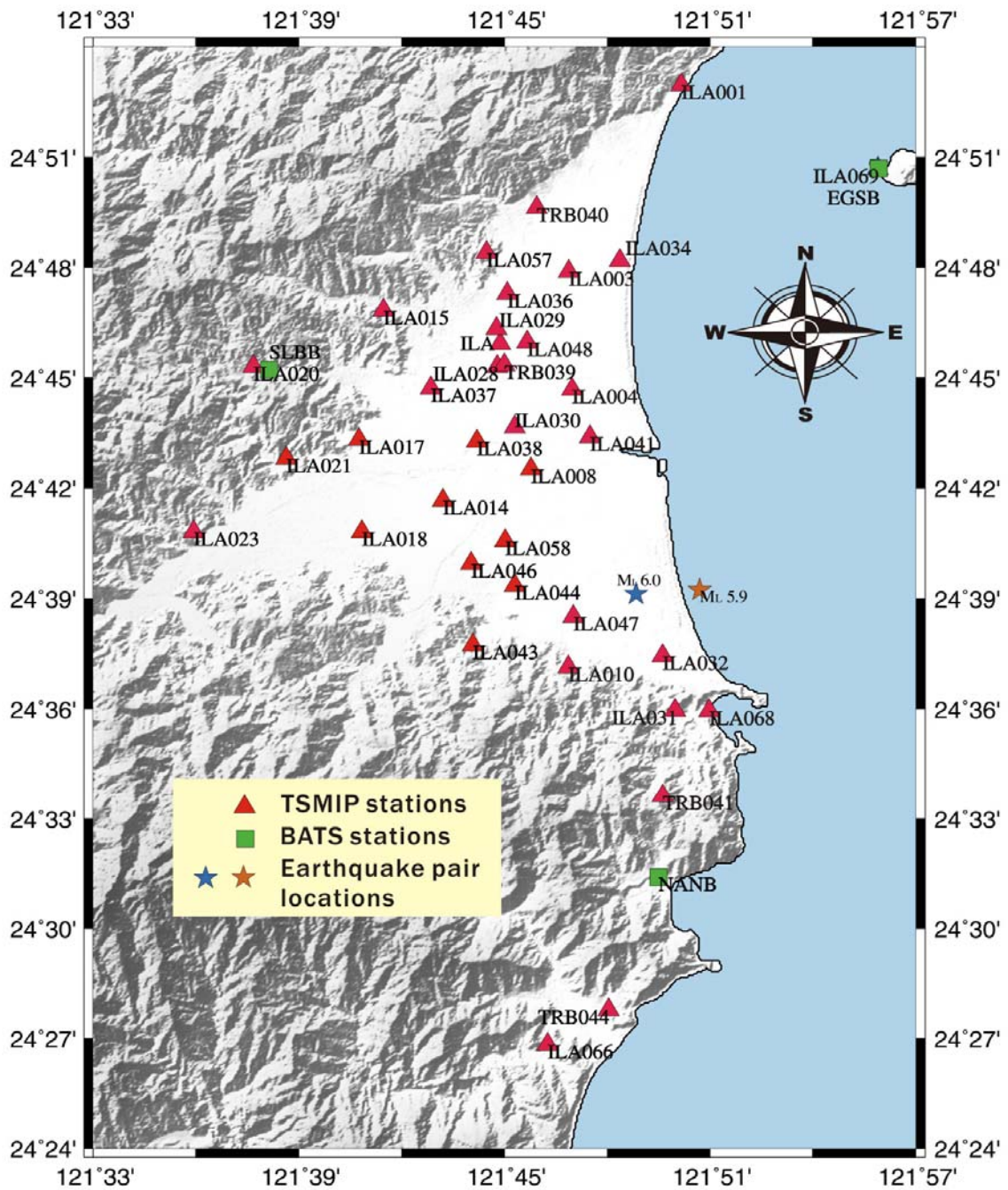


Fig. 13 TSMIP stations in and around Ilan region, with 5 March 2005 double earthquakes hypocenters.

3.3 One Dimension Velocity Model

In order to obtain more accurate local velocity model, we use averaged local velocity layers retrieved from recent tomography result (Wu, et al.,2007). Taking into

consideration of the unknown detailed structure at this region, the latest tomography result would better resolve local velocity structure rather than generalized model obtained from the whole-island, or northeastern Taiwan (i.e. model used by Chou et al., 2006). P and S velocity used in this study are averaged from the tomography grids(in Ilan region; Fig.15) based on Wu, et al.(2007). The horizontal distribution of selected grids are marked as red crosses in Figure 15, and the original setting includes the blue crosses. The original setting takes the center as 121E, 24N. It is divided 7.5 km in x-axis (longitude direction) and 12.5 km in y-axis (latitude direction), with a 20° clockwise rotation from the north. There are 7*5 grids used at each depth with 13 layers vertically from the top. Each layer depth depends on origin setting (depth value at Table.1). Table.1 shows velocity value averaged for each layer. The modified velocity model is taken firstly the averaged velocity from the matrix at the same depth, then added with linear interpolation. We increment more grids in equal space between the depth range of 0~20 km in case to provide intense and smoothed velocity variation. S velocity is re-calculated by V_p/V_s , since in tomography the S-P time is used to consolidate a reliable inversion result. We further modified top two layers of 0.5 km thick to ultra-low velocity. It is to simulate the surface alluvial deposits. Detailed velocity modified for input of moment tensor inversion is given in Table.2.

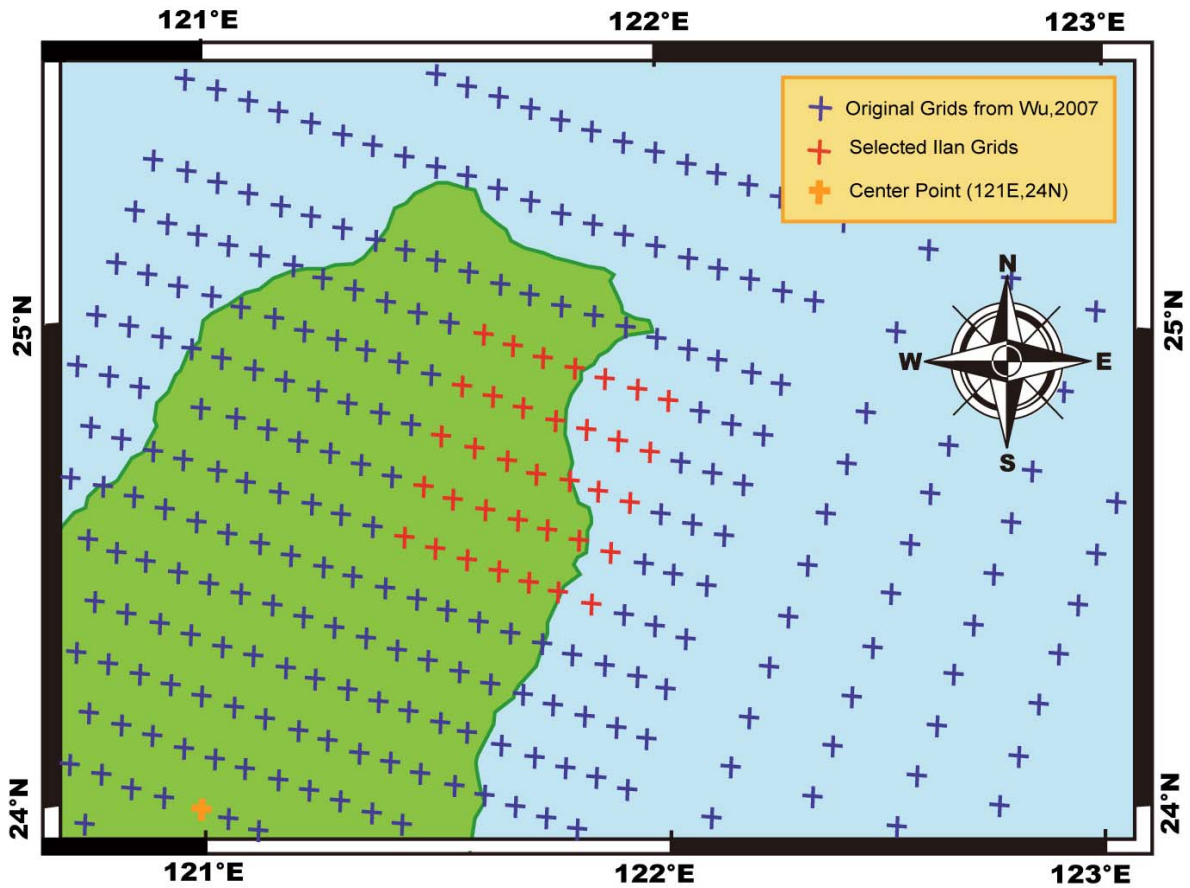


Fig.14 Adopted grids distribution at the Ilan region, the general grid setting please refer to Wu et al.(2007).



Table.1 Tomographic velocity model for Ilan region (Averaged from Wu et al., 2007)

Depth(km)	Vp(km/s)	Vs(km/s)	Vp/Vs
0.000	3.951	2.216	1.783
2.000	4.732	2.766	1.711
4.000	5.214	3.155	1.653
6.000	5.643	3.321	1.699
9.000	5.849	3.321	1.761
13.000	6.011	3.439	1.748
17.000	6.293	3.596	1.750
21.000	6.426	3.657	1.757
25.000	6.460	3.713	1.740
30.000	6.541	3.754	1.742
35.000	6.868	3.921	1.752
50.000	7.808	4.507	1.732

Table.2 One-dimension velocity model modified from Wu, et al.(2007) for Ilan region.

Depth(km)	Vp(km/s)	Vs(km/s)	ρ (gm/cc)	Qp	Qs
0.500	2.000	0.300	1.951	113.000	50.000
1.000	2.865	1.028	2.210	315.000	140.000
2.000	4.595	2.613	2.216	338.000	150.000
3.000	4.906	2.836	2.395	360.000	160.000
4.000	5.062	2.948	2.402	382.000	170.000
5.000	5.132	2.994	2.536	405.000	180.000
6.000	5.201	3.040	2.543	428.000	190.000
7.000	5.342	3.116	2.550	450.000	200.000
8.000	5.483	3.192	2.557	472.000	210.000
9.000	5.624	3.268	2.564	495.000	220.000
10.000	5.712	3.316	2.650	518.000	230.000
11.000	5.801	3.363	2.657	540.000	240.000
12.000	5.889	3.411	2.664	562.000	250.000
13.000	5.977	3.458	2.671	562.000	250.000
14.000	6.047	3.496	2.760	562.000	250.000
15.000	6.117	3.534	2.771	562.000	250.000
16.000	6.186	3.571	2.781	562.000	250.000
17.000	6.256	3.609	2.791	540.000	240.000
18.000	6.325	3.646	2.812	518.000	230.000
19.000	6.394	3.683	2.823	495.000	220.000
20.000	6.463	3.720	2.833	472.000	210.000
21.000	6.532	3.757	2.843	450.000	200.000
26.000	6.842	3.950	2.939	360.000	160.000
31.000	7.292	4.210	3.073	270.000	120.000
36.000	7.906	4.370	3.278	180.000	80.000
41.000	7.942	4.390	3.290	180.000	80.000
46.000	7.978	4.410	3.303	180.000	80.000
51.000	8.231	4.550	3.393	180.000	80.000

In total, 28 layers are set. Below 1 km depth, the vertical division is 1 km. After 21 km depth, the division is changed to 5 km. Vs is obtain from tomography Vp/Vs values. The ρ , Qp, Qs are in reference to CWB, 1-D flat earth model (personal communication).

3.4 *Waveform Data*

All TSMIP seismograms of 5 March 2005 earthquake pair are carefully checked for data quality. Records are previously identified and quality control by CWBSN (C. H. Chang, personal communication). Since there was no equipment to adjust the unit-time base TSMIP records, the accurate time and location of this event is referred to later validation based on relocation process with CWBSN broadband records. We will leave detailed framework of relocation behind since relocation method serves for a minor purpose to this study. Under secondary relocation using hypoDD (Waldhauser & Ellsworth ,2000), the precise time, latitude, longitude, and depth are then justified. We also sampled through and manually picked P arrival to aline complete waveform segments. Continuous data recorded two major events which can be finely separated in 1.08 minutes (Example station ILA042, Fig.16). In the final record format, the displacement is integrated from acceleration data with designed method to balance from baseline drift problem during near field waveform integration. The original sampling rate is 200 bps, and we later adjust it to 50 bps to conform to modified program.

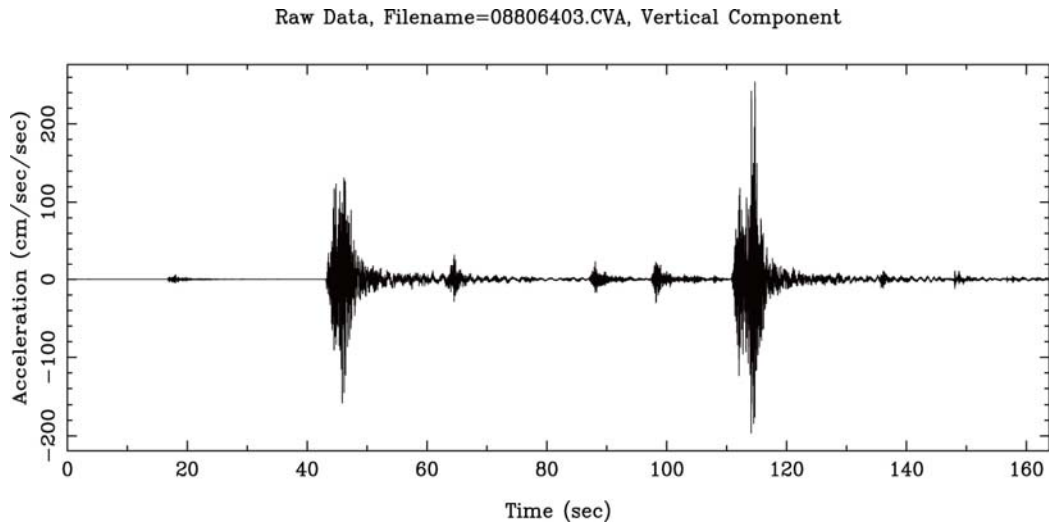


Fig.16 Acceleration waveform from station ILA042. Two mainshocks are well separated in the acceleration seismograph.

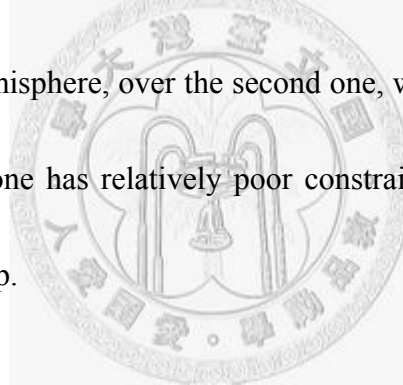
3.5 Synthetic Seismogram Computation

For full application on method described above in Chapter 2.2, we used codes modified from the latest FORTRAN77 program--Computer Programs in Seismology, version 3.3.0 (CPS 3.3.0) by R. B. Herrmann (2002). In this program, waveform synthesis can be derived by three method including generalized ray approximation, wavenumber integration approach, and modal summation. The wavenumber integration approach is taken to instill our ideas. The first modification is that we assembled mhprep96, mhspec96, and inversion kernel as three separate steps. Functions and procedures of them are illustrated in the flow chart in Appendix I. The second modification is that we changed it to be applicable to multi-station inversion. Maximum and minimum limits for station number are case-dependent.

4. Results

4.1 First Motion Solution and Local Aftershocks

Using P wave polarities from CWBSN and TSMIP records, the focal mechanisms of first and second mainshocks were determined as shown in Figure 1 and 2. According to the P-wave first motion method, it categorizes two events into totally different ways of rupture patterns. The first mainshock focal mechanism has better station coverage, in four quadrants of lower hemisphere, over the second one, which provides us confidence to our result. The second one has relatively poor constraint, but it can be determined most as a possible strike-slip.



We also analyzed the first motion focal mechanisms for five $M_L > 4.0$ aftershocks (Figure. 17). It is reassured for minor component of normal involved, and mostly left lateral strike-slip motion. Except for the aftershock at 19:06 and 21:06, they are in between normal and strike-slip pattern, regarding to the rake. The aftershocks are plotted chronologically. And all of them have good constraint on station coverage with the recordings from the CBWSN and TSMIP. More discussion will go on in Chapter 5.

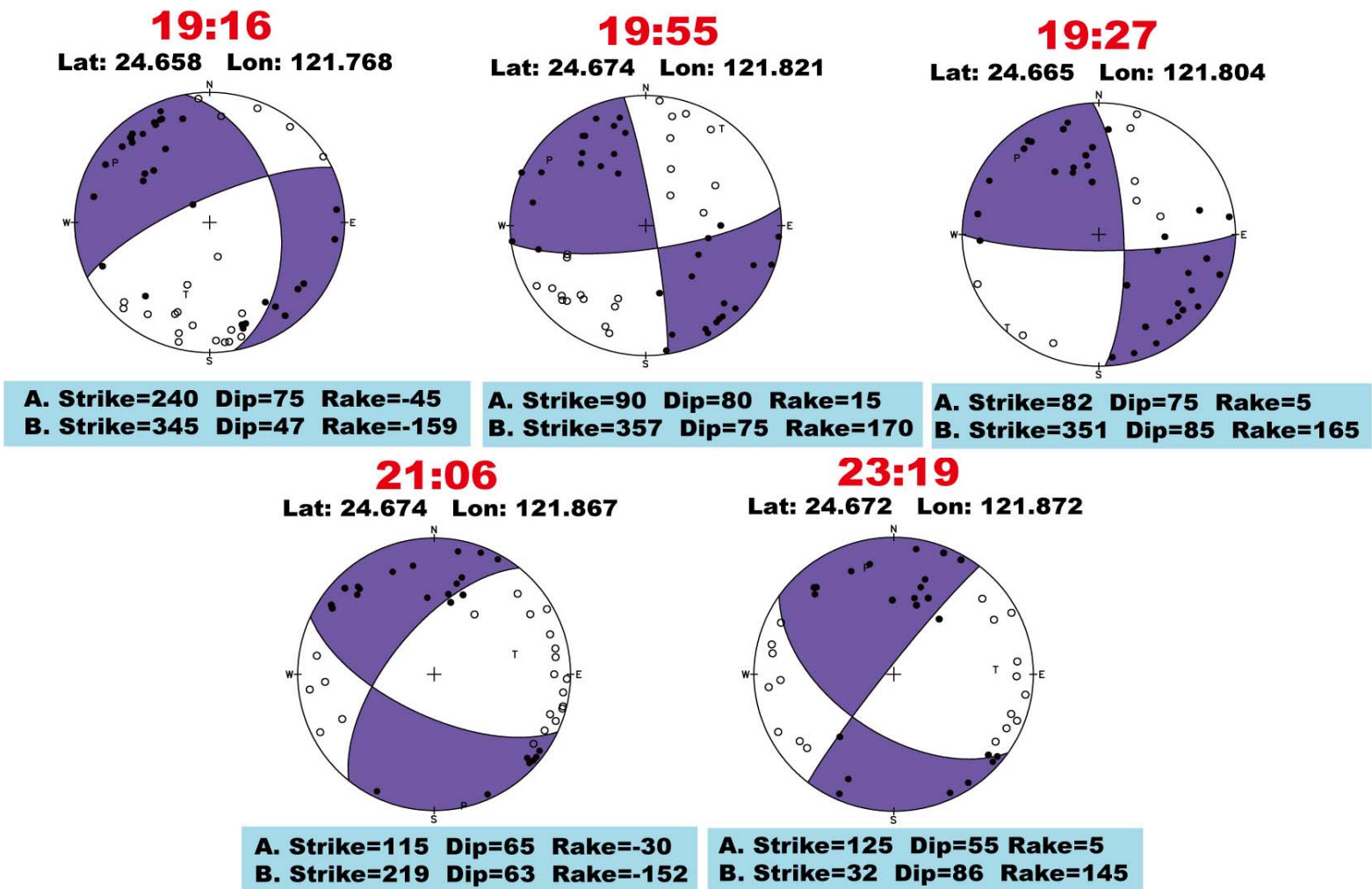


Fig.17 Five focal mechanisms for $M_L > 4.0$ events determined by P wave first motion resolution.

Table.3 Information for each single station and inversed moment tensor result.

ID	CLVD	M _w	Azimuth	distance	Strike1	Dip1	Slip1	Strike2	Dip2	Slip2	χ^2
ILA	7.9	5.43	322	15.47	25.84	37.75	125.46	163.83	60.09	65.81	28.77
ILA001	9.93	5.6	8	24.7	94.77	26.5	3.21	1.89	88.57	116.47	2.55
ILA003	8.69	5.64	339	16.92	73.64	33.98	22.93	324.31	77.42	121.83	53.73
ILA004	17.63	4.61	330	11.67	42.16	43.11	143.85	160.23	66.23	52.92	100.83
ILA005	41.11	2.93	323	6.14	71.52	59.14	9.67	336.52	81.71	148.78	0.0001
ILA008	16.58	5.33	307	9.91	33.61	47.74	174.53	127.29	85.96	42.39	135.30
ILA010	24.85	4.61	233	7.22	336.34	55.5	7.19	242.26	84.08	145.29	1.51
ILA014	44.96	5.31	289	13.11	321.71	52.42	-42.52	80.93	57.61	-133.76	7.16
ILA015	14.55	4.71	313	20.63	36.58	26.68	172.74	133.07	86.75	63.51	3.00
ILA017	0.00	5.41	294	17.92	42.11	53.24	155.34	147.47	70.47	39.42	9.38
ILA018	12.15	4.7	279	16.55	359.24	39.24	152.88	110.88	73.24	53.99	5.14
ILA021	34.22	4.65	287	20.86	159.52	50.28	49.08	33.12	54.43	128.25	6.60
ILA023	17.41	4.63	276	24.69	6.54	37.66	151.93	119.42	73.28	55.72	3.13
ILA028	75.03	4.96	319	14.67	34.6	48.26	51.55	264.62	54.24	124.88	58.42
ILA029	12.27	4.97	324	16.2	21.7	36.9	153.68	133.26	74.56	56.06	50.54
ILA030	16.28	4.78	313	11.81	89.84	75.67	175.79	180.86	85.92	14.36	194.28
ILA031	2.63	4.86	184	6.25	296.59	59.29	4.33	204.38	86.28	149.22	1.57
ILA032	8.89	5.4	196	3.71	291.87	70.3	0.34	201.76	89.68	160.3	565.64
ILA033	0.83	4.99	355	23.32	85.2	22.12	-175.72	351.23	88.39	-67.93	4.09
ILA034	8.36	5.18	348	16.89	80.01	32.35	10.75	340.9	84.27	121.89	38.09
ILA036	8.05	4.71	329	17.35	115.98	40.07	60.67	332.26	55.86	112.39	36.99
ILA037	4.67	5.56	308	16.23	52.22	40.75	173.53	147.14	85.78	49.43	13.84
ILA038	5.99	5.03	304	13	58.81	50.22	176.53	151.04	87.33	39.83	168.17
ILA041	49.25	4.93	327	9.1	91.27	36.56	-112.17	298.16	56.52	-74.36	261.55
ILA043	70.66	5.08	253	11.21	304.08	62.79	-3.93	35.87	86.51	-152.73	1.514
ILA044	77.55	4.71	269	8.69	321.82	29.48	-92.02	144.14	60.54	-88.88	117.15
ILA046	3.71	4.91	268	10.89	358.19	45.04	174.71	91.94	86.26	45.08	7.129
ILA047	30.11	4.86	252	5.65	302.66	67.67	163.7	39	74.95	23.17	10.80
ILA048	44.02	5.65	327	14.75	49.09	45.82	34.24	294.12	65.78	131.36	66.49
ILA057	4.48	4.57	329	19.64	39.1	50.92	-162.26	297.69	76.32	-40.46	2.37
ILA058	16.05	4.66	283	9.1	301.47	43.07	-113.17	151.84	51.11	-69.8	94.21
ILA060	33.7	4.64	181	9.0	268.30	48.03	7.38	173.35	84.52	137.79	2.86
ILA068	6.97	4.83	170	6.2	274.2	60.02	5.25	181.57	85.45	149.91	1.28
ILA069	24.7	4.68	25	22.69	123.61	36.63	167.25	223.9	82.43	54.06	7.14
TRB039	30.03	5.05	320	14.58	33.71	48.62	13.59	249.63	79.84	137.81	53.55
TRB040	8.35	4.87	338	20.55	57.21	25.67	174.38	152.27	87.57	64.44	5.13
TRB041	7.28	4.89	186	5.72	277	61.56	-0.63	7.3	89.44	-151.56	1.59
TRB044	7.47	5.19	190	21.55	277.06	29.05	3.74	183.79	88.18	119	0.62

The green shaded rows are stations selected for the multi-station approach.

As the result presented in Figure 18, each station has great fitting between synthetic and observation waveforms. All of the plotted solutions are those with CLVD less than 10 %. Low CLVD percentage suggests better agreement to a shear slip fault rupture rather than a volume-change pattern. Red lines are synthetic and black lines are observed displacement waveforms with a band-pass filter. The results take more left lateral strike-slip motion in south of Lan-yang drainage. On the contrary, results are inconsistent at northern part, even though better waveform fits are general to all stations. Station information relevant to this event is listed in Table 3. Obviously, results suggest that inversion on single station would provide ostensible but well-agreeable fitting on waveform. Whereas this gives a rather fussy constrain to obtain single focal mechanism. No common agreement occurred to resemble one centroid moment tensor. This therefore intrigues us to jointly use multi-station approach to obtain a stabilized and reliable result.

4.3 Moment Tensor Solution—Multi-Station Result

The multi-station approach yields one inversion mechanism with joint fifteen stations, and the station locations are shown in Figure 19. The result is empirically tested with fitting frequency and hypocenter location parameters (Chapter 2.6).

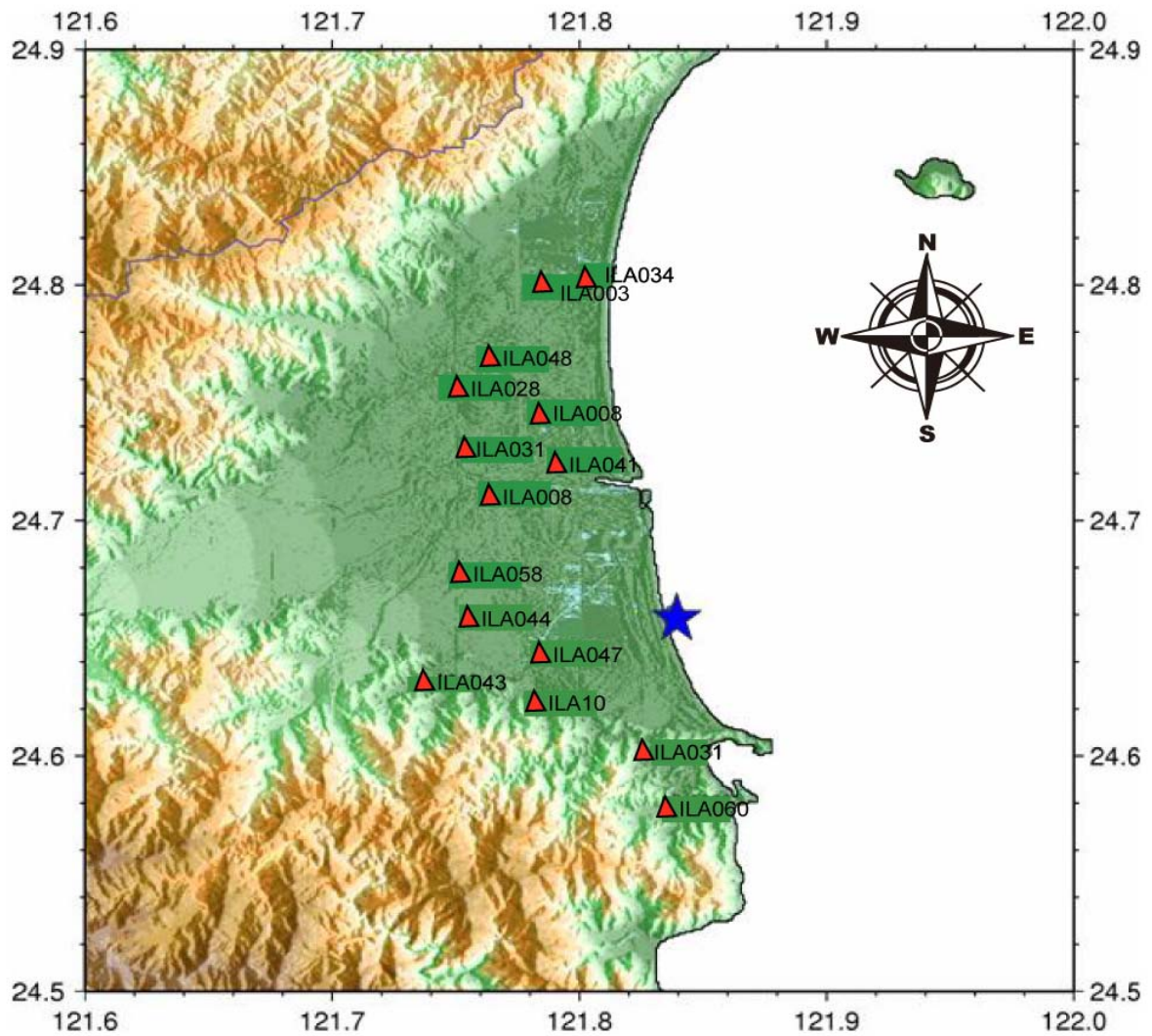


Fig.19 Station distribution for multi-station inversion test. Stations (red triangles) offer a well coverage larger than 180 degrees in azimuth for the first mainshock (blue star).

Inversion result suggests that a left-lateral strike-slip pattern, but some normal component is also involved (Fig. 20) The inversion result is based on focal depth 10.6 km and epicentre E121.8°, N24.5°. With a rake of -39.3°, the slip is in between strike-slip and normal dip slip. As we can see from misfit χ^2 index, it is rather large misfits on waveform (Fig. 20). In comparison with the single station approach, the waveform misfits are relatively high. However, this sufficient trade-off is expected in

multi-station approach, since it accounts to render one result for more station records.

And the consistency of this solution is further examined in the depth test. Please refer to

Chapter 5.2 for further discussion.

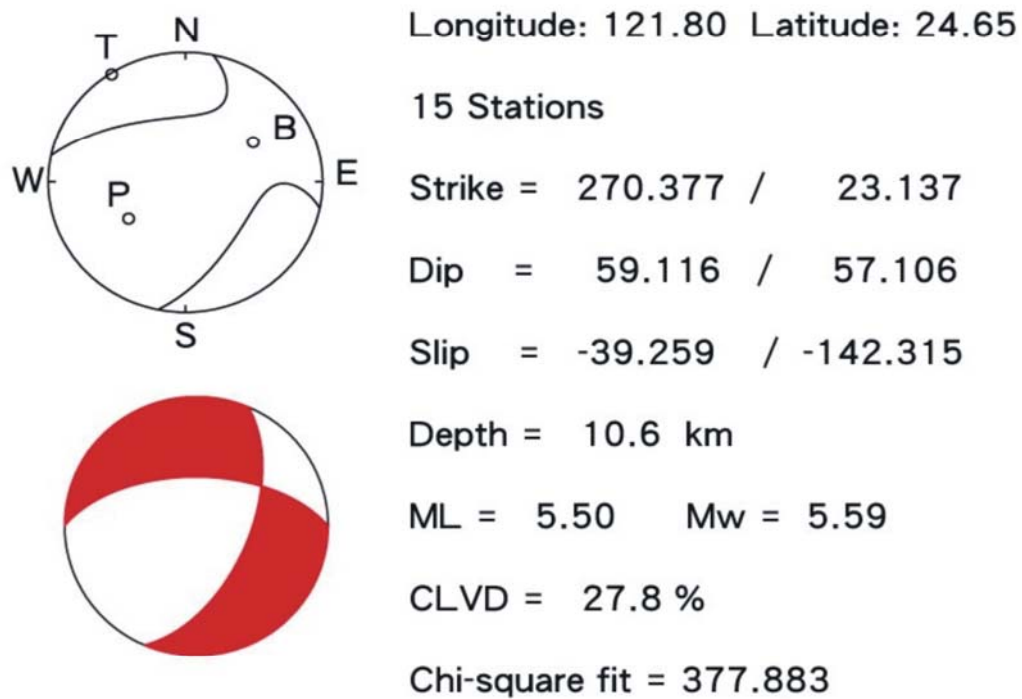


Fig.20 Joint inversion result using focal depth of 10.6 km (Refer to Chapter 5.2.1 to obtain more information of the depth test)

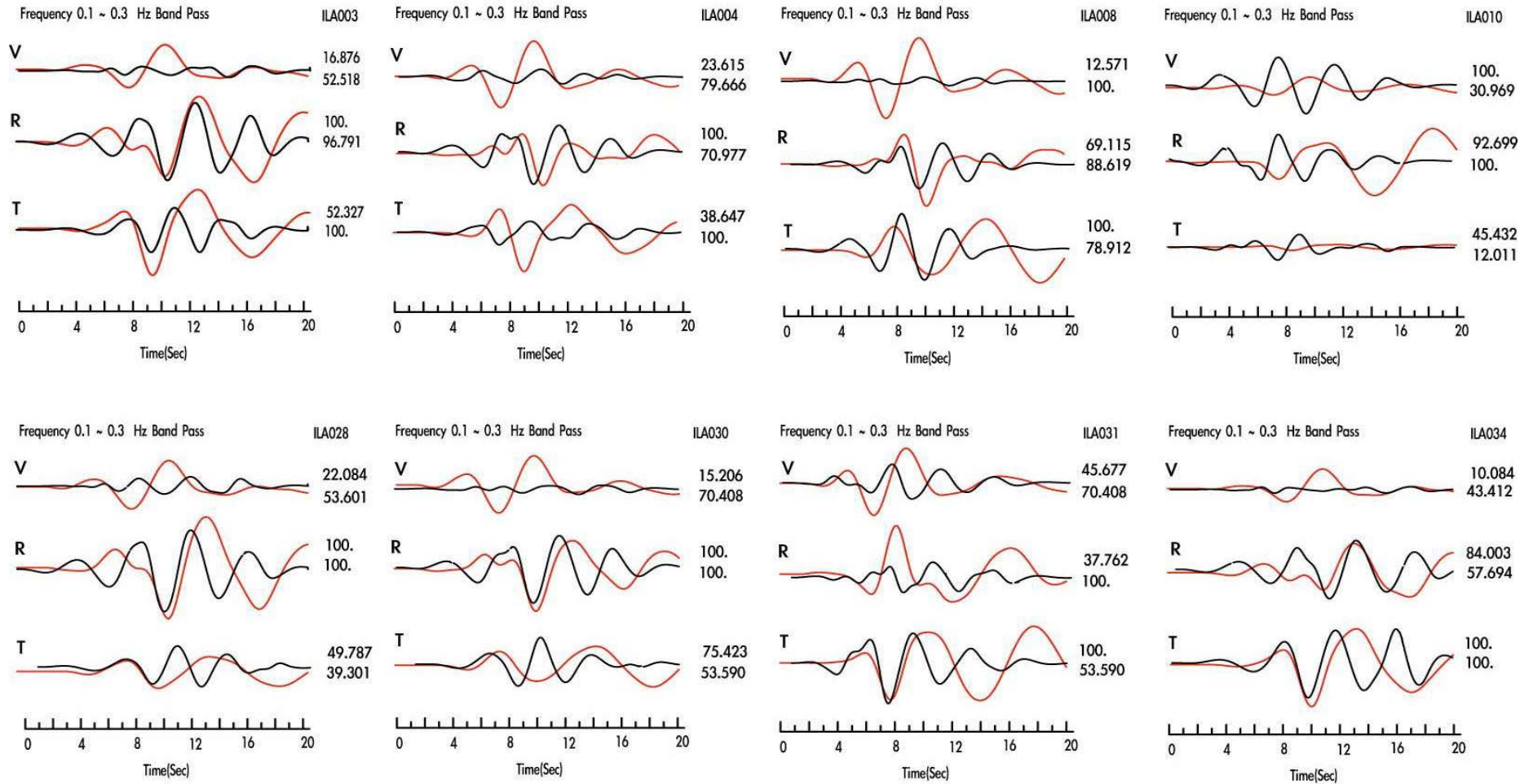


Fig. 21 Waveform fitting from 15 stations inversion, the fitting range is within 20 seconds under adjustable time shifts. Black curves represent observation records while red curves represent synthetic simulations. The numbers given beside waveform are percentage in accordance to maximum amplitude among components, which is compared separately on observation and synthetic.

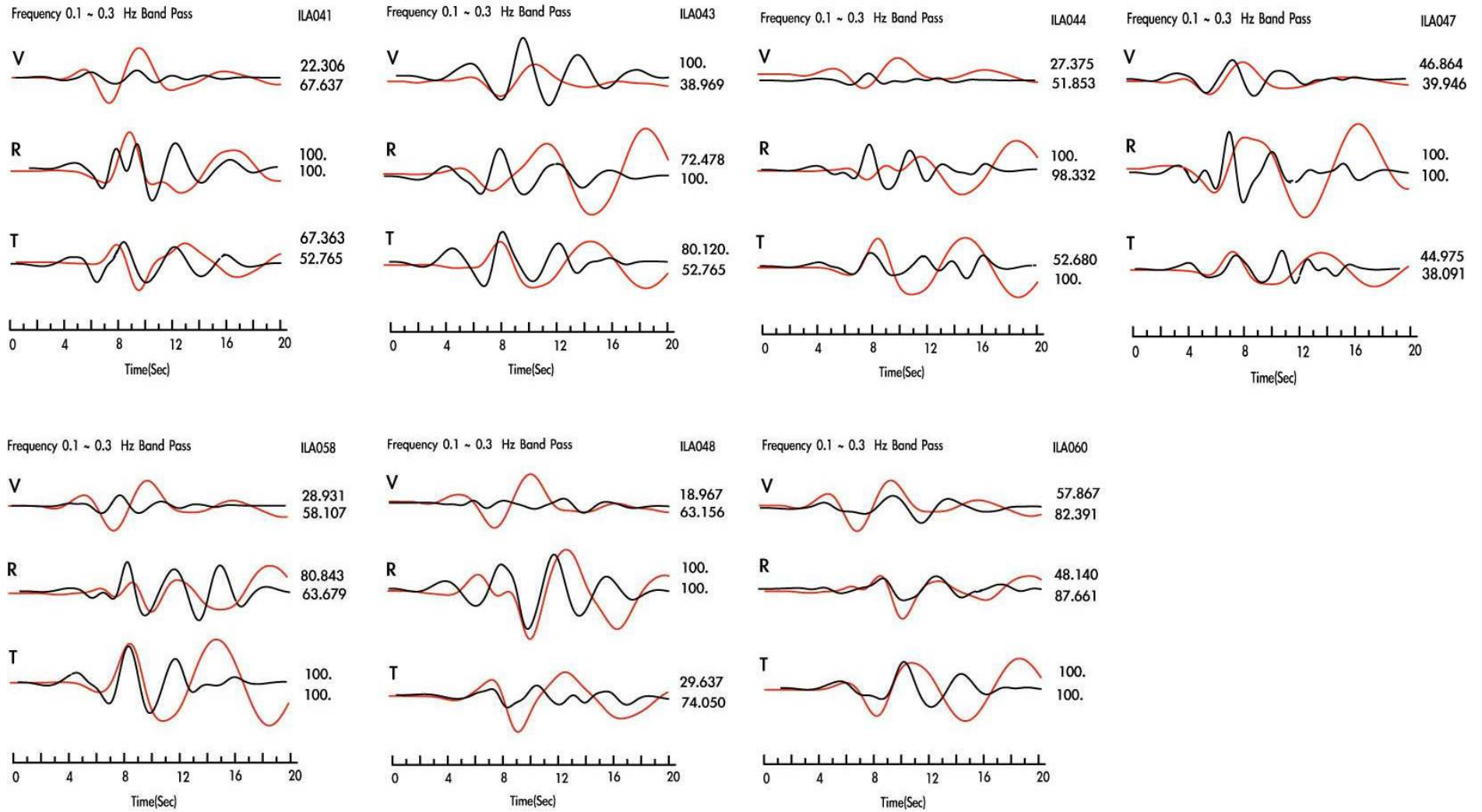


Fig. 21 Caption refer to last page.

5. Discussion

5.1 Single Station Inversion

5.1.1 Tradeoff Problem

Although the ostensible goal for a waveform inversion solution is to successfully fit the observation, the most obligatory demand under agreeable assumption is to derive a correct moment tensor. In the procedure of inverting source moment tensors, several parameters constrain the effect of synthetic waveform generation. As we ever deduced in Chapter 2, (2-2-1-5), it contains medium effect-- the velocity structure, and the variables on moment tensors. In short, there are two means to improve waveform misfit. In a way, one could use a refined velocity model to calculate the Green's function, which is usually an approximated solution gained from different empirical studies. In the other, low-frequency band pass is applied in compatible with the simple velocity structure (Kao et al., 1999). However, near-field array in this study has higher sampling rate(maximum 200bps) and offer more information on waveform resolution, which is an advantage. To adopt such advantage, there is no reason for us to lower the fitting frequency range.

The inconsistency of near-field, single station results can be explained by such

tradeoffs. For the tradeoff between two portions mentioned above, simple ideas shown in Figure 20 well explain the phenomenon (Douglas et al., 1985). Any incorrect description, like the hypocenter depth (affecting $g(t)$) or focal mechanism(affecting $m(t)$), would result in creating a Green's function different from the "true" one. When an incorrect Green's function is convolved with the "true" source function, the resulting seismogram will, in general, differ from the "true" seismogram. Vice versa, an incorrect Green's function can be compensated with another incorrect focal mechanism solution , in order to generate waveform similar to observation (Figure 22, Douglas et al., 1985). If improper Green's function is set, we would become ignorant about in which portion the error occurs, and vulnerable to the focal mechanism derived from it.

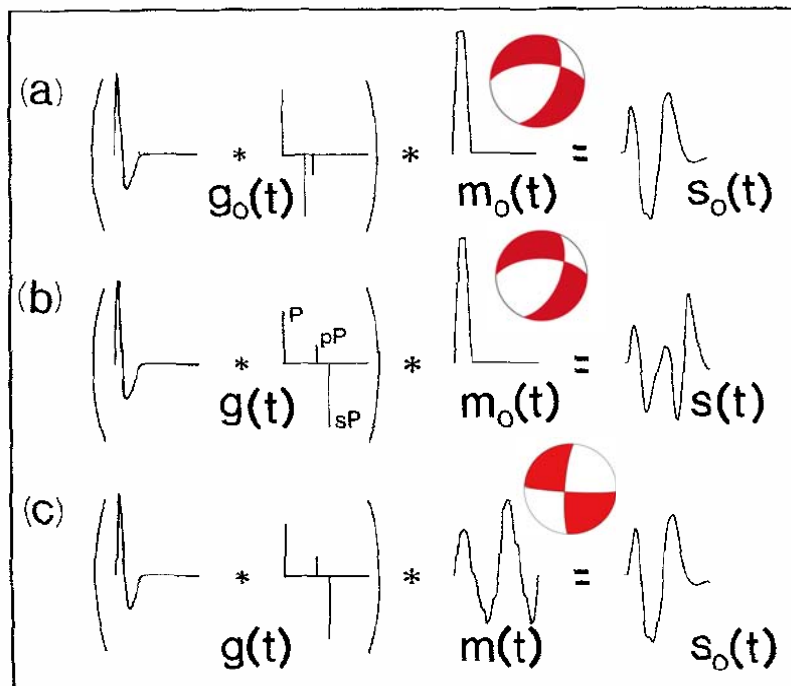


Fig.22 Schematic example of the trade-off between the Green's function and the source pattern (Douglas et al., 1985). In (a) through (c), the Green's function has been separated into two functions. Green's function combines of the instrument and

attenuation operators, and source function is a sequence of delta functions that depend on the focal mechanism and depth. **(a)** $s_0(t)$, the observed seismogram, shown as the convolution of the "true" Green's function, $g_0(t)$, and the "true" source function, $m_0(t)$. **(b)** Assuming an incorrect Green's function, $g(t)$, is illustrated. The convolution of $g(t)$ with the "true" source function, $m_0(t)$, produces the incorrect seismogram, $s(t)$. **(c)** The trade-off between two functions, $g(t)$ and $m(t)$, is demonstrated. The convolution between the two incorrect functions can still be capable of producing the "true" seismogram, $s_0(t)$.

Also, hypocenter depth and location assumption affects the portion of Green's function (Douglas et al., 1985). Resembling to earthquake relocation problem, these tradeoffs can be eliminated or diminished by multi-station inversion. To refine localized approach, more station data and well coverage of the stations are both important. When probing further to higher frequency, more details would be involved in the inversion. Those factors simultaneously affect the stability of solution. All the effects will be described separately in the following sections.

5.1.2 Sensibility to Velocity Model

Kao et al.(1999) proposed that main effect of choosing different velocity models for different stations is to improve the waveform correlation rather than to alter the solution. Our single station approach agrees well with this statement, yet with a much more simplified test of half space model. We can see from Figure 18 in Chapter 4, that even with most simplified model, each station record fits well to the observed. This

corresponds to the explanation in Figure 22. Most velocity variation can possibly be absorbed by the distortion on moment tensor. Therefore, there is no consistent inversion result to support a single event. Rather, results changes abruptly at north part, where the stations situated in soil sites with great velocity variation underneath (Fig. 28). The velocity is sure to deviate from the simple model set for single station approach (Fig.18). Local geological settings proposed by previous studies (Chapter 1.2, Fig. 6-8) have implied possible velocity uncertainties at the northern stations. On the contrary, five consistent focal mechanisms in southern part indicate overall left lateral strike-slip motion for the first mainshock. These sites are mostly located at rock sites. It can be inferred that the simpler the real structure is, the more accurate and stable the waveform solution is. Single station inversion was undermined by such complex structure underneath Ilan plain. We had tried some trail tests to modify the half-space model to layer model. However, the modification of 1-D velocity somehow improved the waveform fit to the best (0.3~0.5 Hz fitting) , but left the reasonable focal mechanism behind.

5.1.3 Solution to Single Station Problem

Possible solution to single-station problem lies in combined inversion of regional seismic network to average out complications. It is onerous to access an

“accurate” regional velocity model, and even more arguable to verify the accuracy of it to each path. There are studies that had experimented on joint-inversion technique for local earthquakes (Tan et al., 2005). On the contrary, these applications are done in the regions with much simpler velocity structure.

5.2 Multi-Station Inversion

Solving waveform inversion with more than one station has been proposed and tested as a good way to remedy anomalies on Green’s function in different ray path. It would sufficiently retrieve reliable source parameters (Tan et al., 2005). Even if it is much appropriate for smaller events to be compatible with the point source assumption, we realized, in our study, that this application on the threshold magnitude ($M_w = 5.9$) can also track the average slip motion from our multi-station approach. Since this joint inversion result remains stable and correlates well with local historical mechanisms, the normal component of this event corresponds to our P wave first motion solution. Possibly, the better station coverage and great differences in velocity model contribute to this solution.

5.2.1 Depth Test

We later verify the trade-off between focal depth and waveform misfit which is widely known problem for the inaccuracy on hypocentre location, at our multi-station approach. The depth test is done from 6 to 14 km with fixed epicenter (Fig. 23, Table. 4). This calibration range in vertical direction is plausible under the credit of relocation error tests (Chang, 2004). It was to determine the best solution with lowest misfit and compensated linear vector dipole (CLVD) percentage. Low CLVD percentage is quite representative to a shallow and simple slipping source. Thus we prefer lower value of it. But, it is also possible that the event behaves as a complex source, and therefore posses higher CLVD. It is clear from the mechanisms drawn on one single lower-hemisphere map, that most solutions are set close together. The results tend to strike-slip pattern at shallow (6 km) or deeper (14 km) depth, but more normal component around 10 km, which is close to the depth value given by relocation (10.54 km). Somehow, variation in all trails is rather small (Fig.24). It provide proof for the stability on our multi-station approach. The optimum solution at 10.6 km minimizes both waveform misfit and the CLVD percentage in this event.

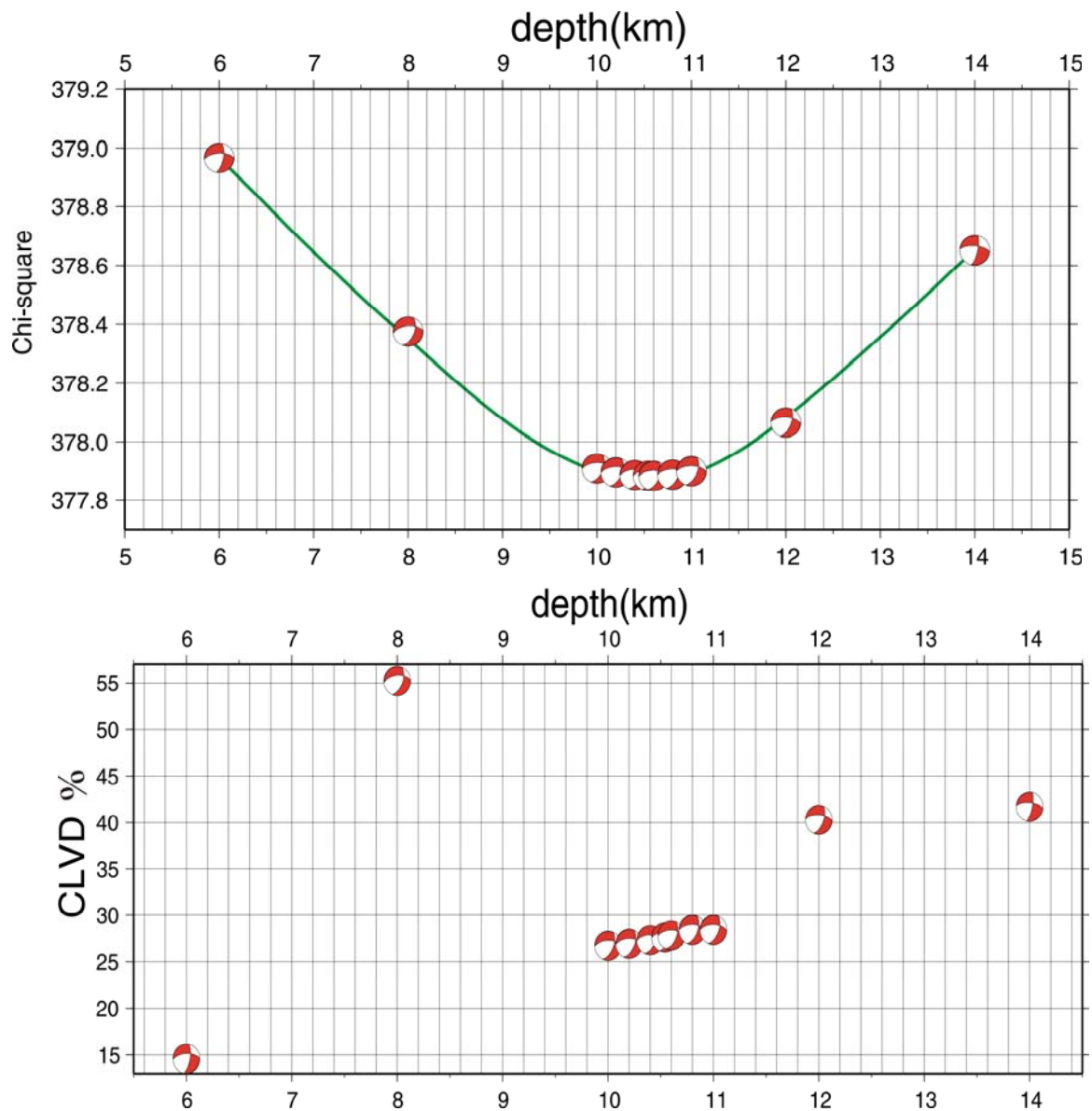


Fig.23 Depth test corresponds to optimize inversion misfit and CLVD percentage. Lower hemisphere centroid moment tensors (CMTs) are demonstrated on the plot. The calibration is relatively small in fault geometry change. Plausible reduction on misfit and CLVD percentage confirm focal depth as around 10.54 km, finely correspond to relocation result. Upper panel presents that the waveform misfit χ^2 index varies with depth, and reaches the lowest point at 10.6 km. Lower panel presents variation of the CLVD percentage. It also turns to a lower point around 10 km.

Table.4 Focal depth test parameters, fault plane geometry and motion result.

Depth (km)	χ^2	strike1	dip1	slip1	strike2	dip2	slip2	CLVD	Mw
6.00	378.9662	267.85	61.63	-25.86	10.82	67.43	-149.03	14.60	5.24
8.00	378.3748	265.01	56.75	-42.07	21.35	55.92	-138.55	55.20	5.40
10.00	377.9094	268.67	58.12	-41.22	23.50	55.98	-140.41	26.70	5.56
10.20	377.8957	269.27	58.46	-40.57	23.40	56.34	-141.06	26.90	5.57
10.40	377.8864	269.84	58.79	-39.91	23.28	56.72	-141.70	27.30	5.58
10.54	377.8846	270.22	59.01	-39.46	28.18	56.99	-142.12	27.60	5.59
10.60	377.8834	270.38	59.11	-39.26	23.14	57.11	-142.32	27.80	5.59
10.80	377.8881	270.89	59.44	-38.59	22.97	57.51	-142.93	28.40	5.60
11.00	377.8995	271.21	59.59	-38.25	22.96	57.72	-143.23	28.40	5.62
12.00	378.0652	273.47	61.44	-33.99	21.33	60.59	-146.72	40.30	5.66
14.00	378.6518	275.01	65.49	-18.12	12.74	73.56	-154.37	41.70	5.79

Orange shaded rows indicate the dense grids around relocation result, 10.54 km, testing for rather precise resolution.

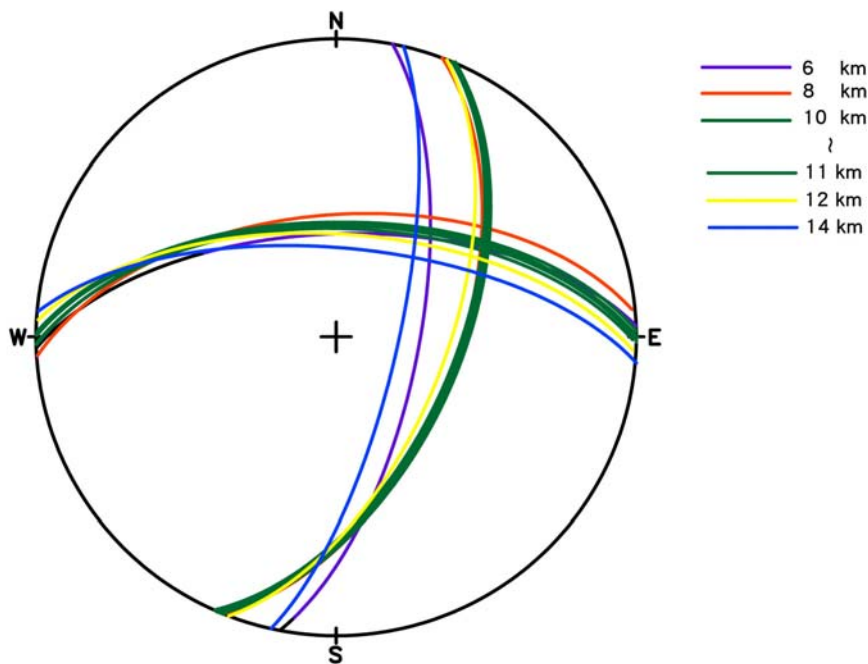


Fig.24 Fault plane geometry variations for the depth trade-off test. The calculated fault planes are finely concentrated to a fixed domain. This is a good demonstration that centroid moment tensor solution is well consistent.

5.2.2 Comparison with BATS

5.2.2.1 Focal Depth

As we see from the Depth Test in previous section, the inversion results yield strike-slip when the focal depth is set as shallow as 6 km and as deep as 14 km. This might implies that the focal depth choice of BATS, the optimum 20 km, was much too deep for approximating this event (Fig.2). It yields the result of a rake -10.25° . On the other way, the poor resolution for shallow earthquake, derived from intrinsic velocity model setting, brought up the minor error in CMT solution.

5.2.2.2 Station Coverage

In comparison with BATS network, the TSMIP arrays have better coverage than BATS. The first mainshock triggered 99 stations in total for the whole Taiwan area, and 38 of them are within the selected Ilan region. For the multi-station approach, the 15 stations used obviously formed a well coverage of 167° , nearly occupying two quadrants of the lower hemisphere (Fig.25). That is the best station distribution obtained for the coastal epicenter of the first mainshock. The result of joint inversion may also be affected by the station coverage. Satake(1985) proposed that error on moment tensor inversion would vary significantly with the combination of fault mechanism and station

distribution. Since our selected stations were more uniform than BATS, the normal component may as well be resolved.

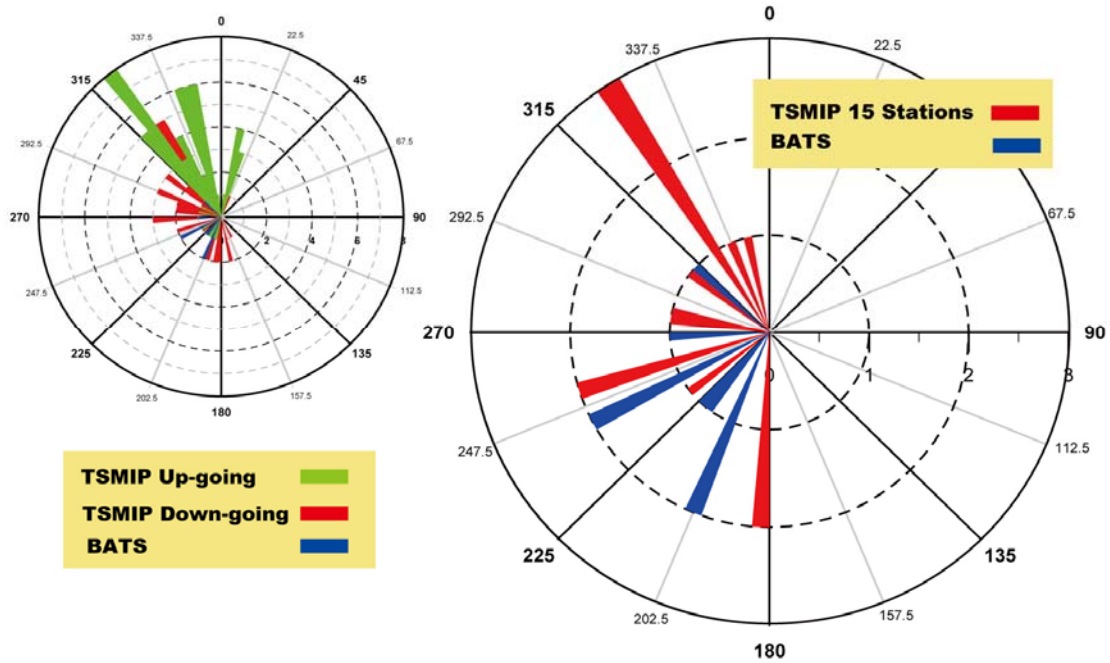


Fig. 25 Station coverage in the azimuth rose plot, radius represents station numbers. Left panel are the involved station records from TSMIP and BATS for the first mainshock. The right panel is the stations used for multi-station inversion approach both from TSMIP and BATS.

5.2.2.3 Velocity Model and Frequency Range

Although the simplified velocity model used in BATS solution is selected as a *priori* to fit long-period data, it was reduced from Rau and Wu (1995) averaged 1-D model (Fig. 26). The simplified approach is appropriate to simulate large events ($M_L \geq 4.5$) and inapplicable to smaller events, which lack long-period signal. It would be contrast to our modified detail velocity structure designed to model waveforms, when reaching higher frequency band. To fit the near-field and high-resolution seismogram,

we construct detailed local velocity model from latest tomography (Wu, 2007). This tomography result has reasonable responds at the shallow depth with a V_p and V_p/V_s negative anomaly, which corresponds to the Ilan plain structure. And we modify 2 km of the shallow part as $V_p=2.0$ km/sec, $V_s=0.3$ km/sec corresponding to the plain structure.

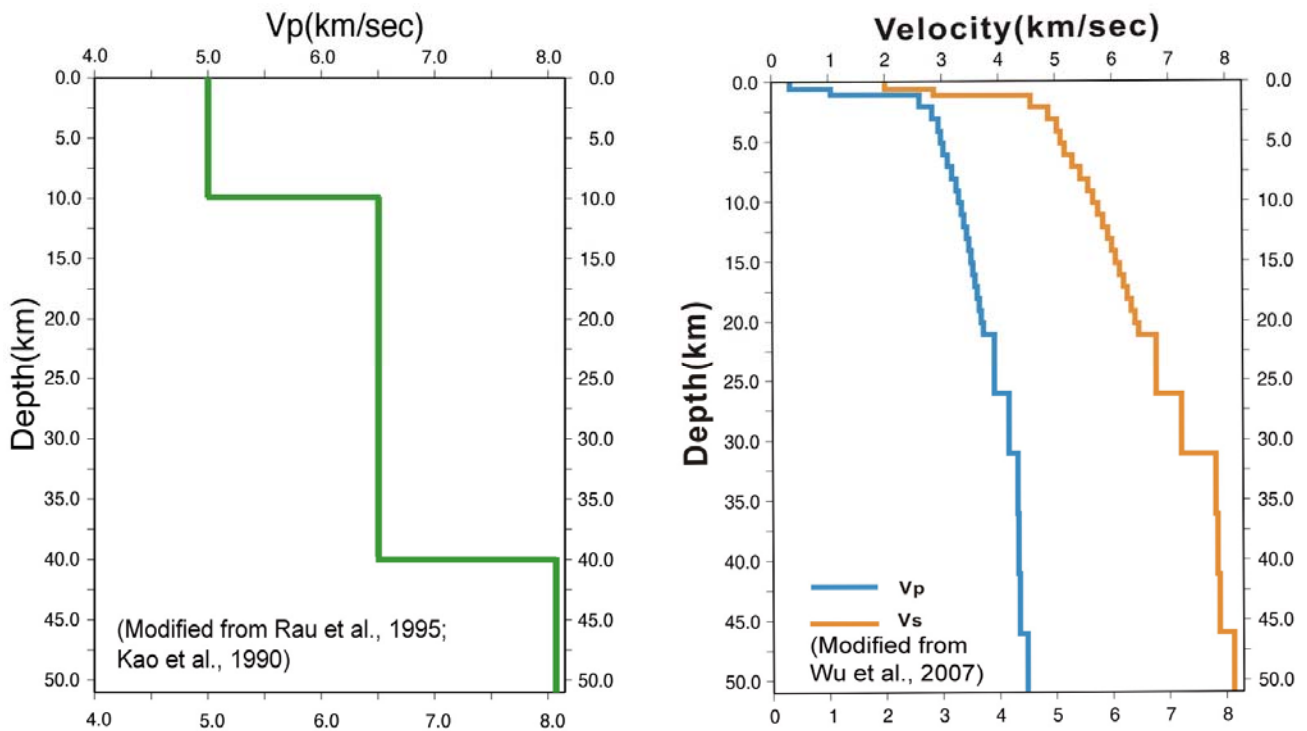
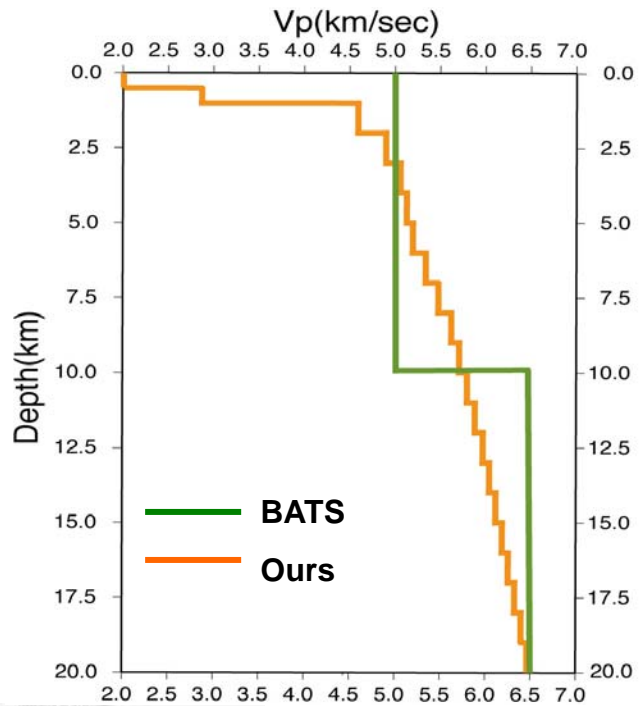


Fig.26 Velocity model used for BATS CMT inversion (left panel) and our modified velocity model (right panel) from Wu(2007). For fitting low-frequency waveform, a simple layer model is suitable. For near-field records, local velocity is specifically designed for the study region. Two of them can be abruptly different.

To compare with BATS velocity model, two velocity models contrast most at the depth of 10 km, where BATS set the boundary of the top two layers (Fig. 27). Our modified model has smoother velocity variation around this depth, and still confirms an optimum result at 10.6 km. From the tomography, there is no such boundary commonly

existing in Ilan region (i.e. profile in Figure 28). It is possible that such dramatic setting on BATS velocity model biased the normal component for an event depth around 10 km, in Ilan region. Around this depth range, solutions are inconsistent on



waveform fit. Therefore the optimum solution of BATS went down to the depth of nearly 20 km to satisfy the inversion, but CMT

Fig. 27 Comparison on velocity models between BATS and ours, from the surface to depth 20 km, with only the P wave velocity. Only the shallow part above 12 km would matter for a short-distanced ray path with an epicenter around 10 km. However, the greatest contrast is around 10 km.

solution was well affected on rake. The normal component is lost for a deeper epicenter.

In other words, BATS obtained a strike-slip component purely for the over-generalization of large-scale velocity model, to the local region as complex as Ilan.

Demonstrating two profiles from the tomography, it is clear that velocity variation is drastic underneath the Ilan plain (Fig. 28). In the profile A'A and B'B, there are no common velocity boundaries around 10 km. Rather, it shows inhomogeneous changes especially of P velocity at the north portion of the Ilan region. These profiles therefore convince us to the application of the averaged velocity model in multi-station approach.

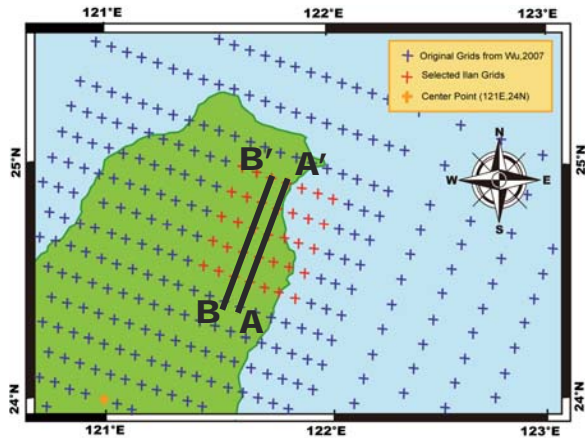
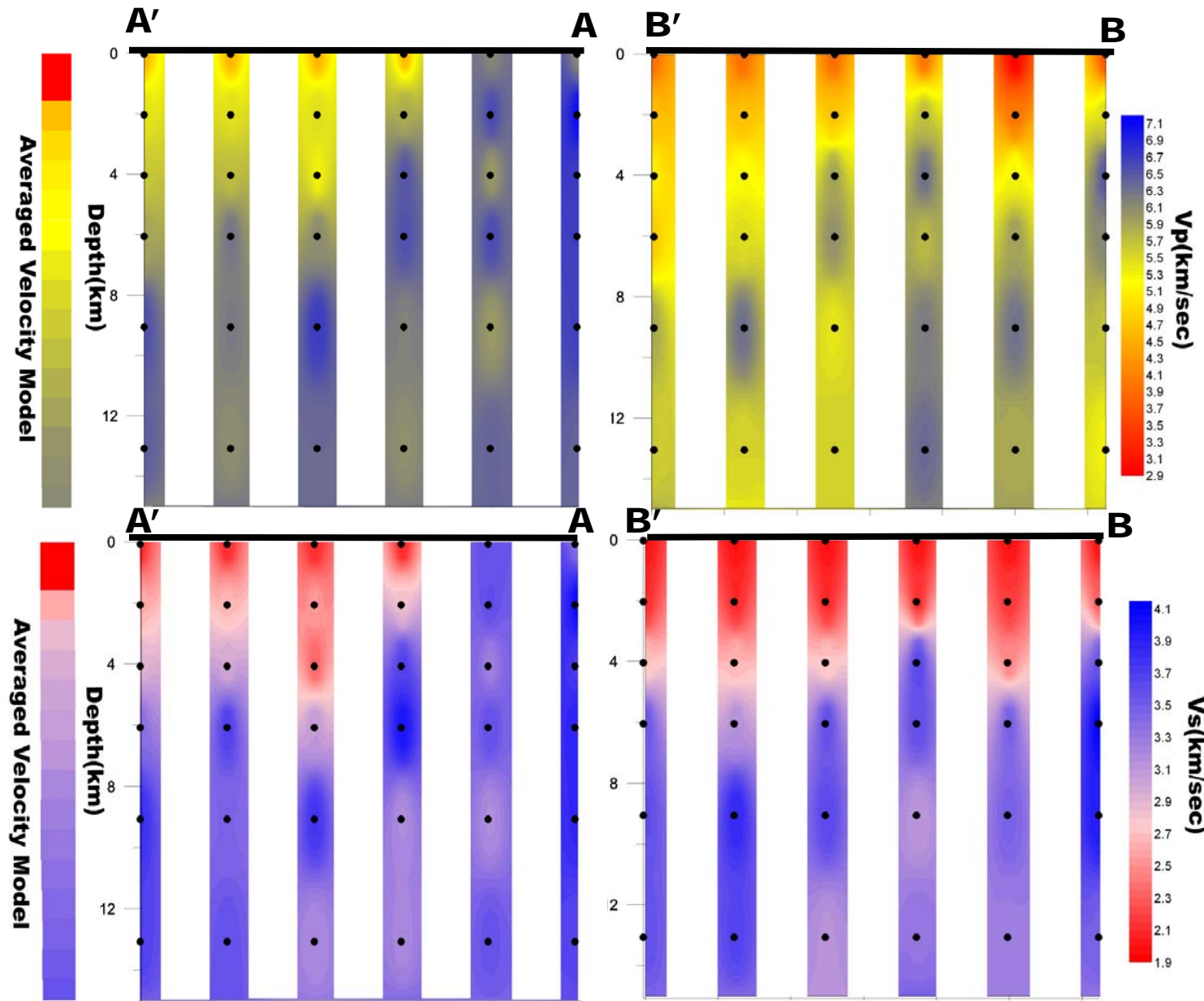


Fig. 28 Two profiles showing the tomography structure underneath Ilan plain—A'A and B'B (shown above). They each cross 6 grids horizontally in NE to SW direction. At the right, P wave velocity is at top panels and S wave velocity at the bottom. Black dots are where grid values exactly locate. Color bars for the profiles are columns at the right, showing independently the P and S velocity grading. The variations on the profiles are 2nd interpolation from black dots, color fill contoured. The averaged velocity models given in multi-station approach are drawn as the columns in the left to be in contrast.



If it is not from the effect of velocity boundary, it would be for such high frequency information resolvable only by local short-period records. Broadband records in a distance more than 100 km lost most high frequency information relevant to initial ruptures, which contain mostly the normal component.

5.3 Local Clustered Aftershocks

Using temporal and spatial linking method, empirically designed threshold of 3 days and 5 km to cluster the seismicity, the 5 March, 2005 earthquake pair is tailed by 605 aftershocks. The aftershocks distribute linearly along a trend of N80°E strike, and virtually shape a flat fault plane (Fig. 27). Even if the simulated fault plane is only for demonstration, we can see the inversion result agrees fairly well with the strike, and also nicely with the dip. On the other hand, the first motion mechanism agrees simply to the dip angle, and possibly it is more representative to a initial rupture with slightly different strike and rake direction.

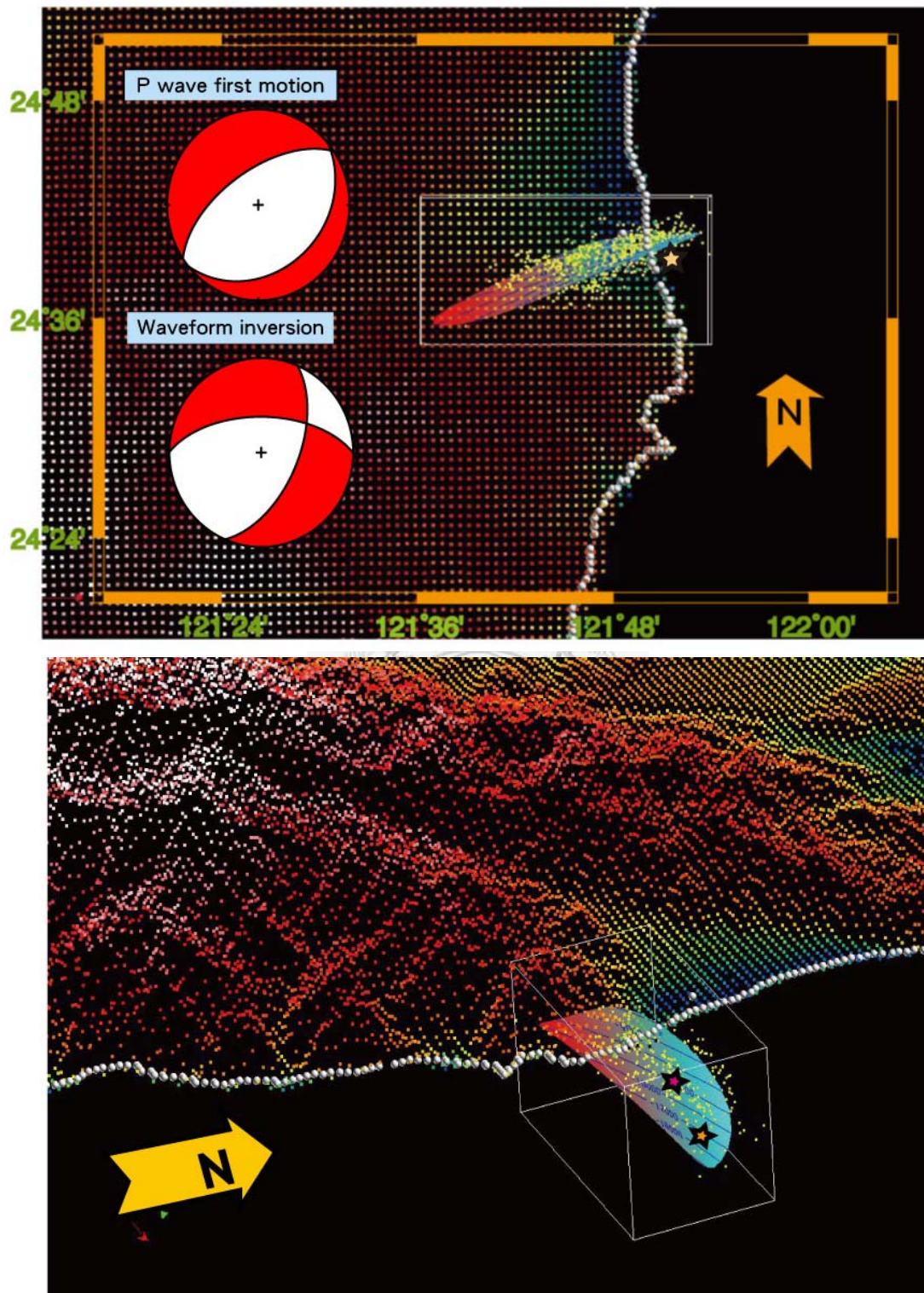
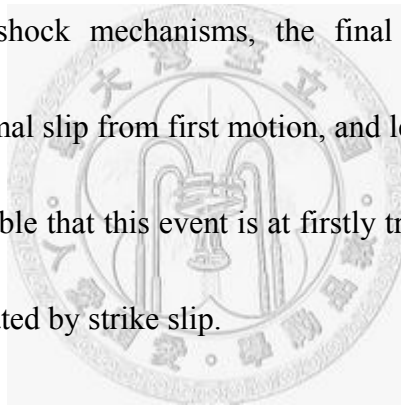


Fig. 29 5 March, 2005 aftershock distribution and fitted fault plane by Gocad (National School of Geology (ENSG) in Nancy, France). The simulated fault plane is mainly for demonstration. We can see in three dimension the distribution of aftershocks and proposed fault plane. The lower panel shows a different viewing direction. Orange star represents the first mainshock, and the pink star is the second mainshock.

We further selected five aftershocks from the cluster to reveal the detail rupture pattern for this series, and compare with our inversion result. These aftershocks are selected for their good condition of station coverage on first motion mechanisms (Fig.30). Magnitudes are all above 4.0. In Figure 30, we can see aftershocks chronologically lined up from west to east, and all of them possess left lateral strike-slip component. The first aftershock(1) resembles much with the mainshock on the minor normal component. The rest two(No. 2 and 3) agree with the mainshock on fault strike. On consideration of aftershock mechanisms, the final result of our multi-station approach is in between normal slip from first motion, and left lateral strike-slip from the aftershocks. It is most possible that this event is at firstly triggered with a minor normal motion, than mostly dominated by strike slip.



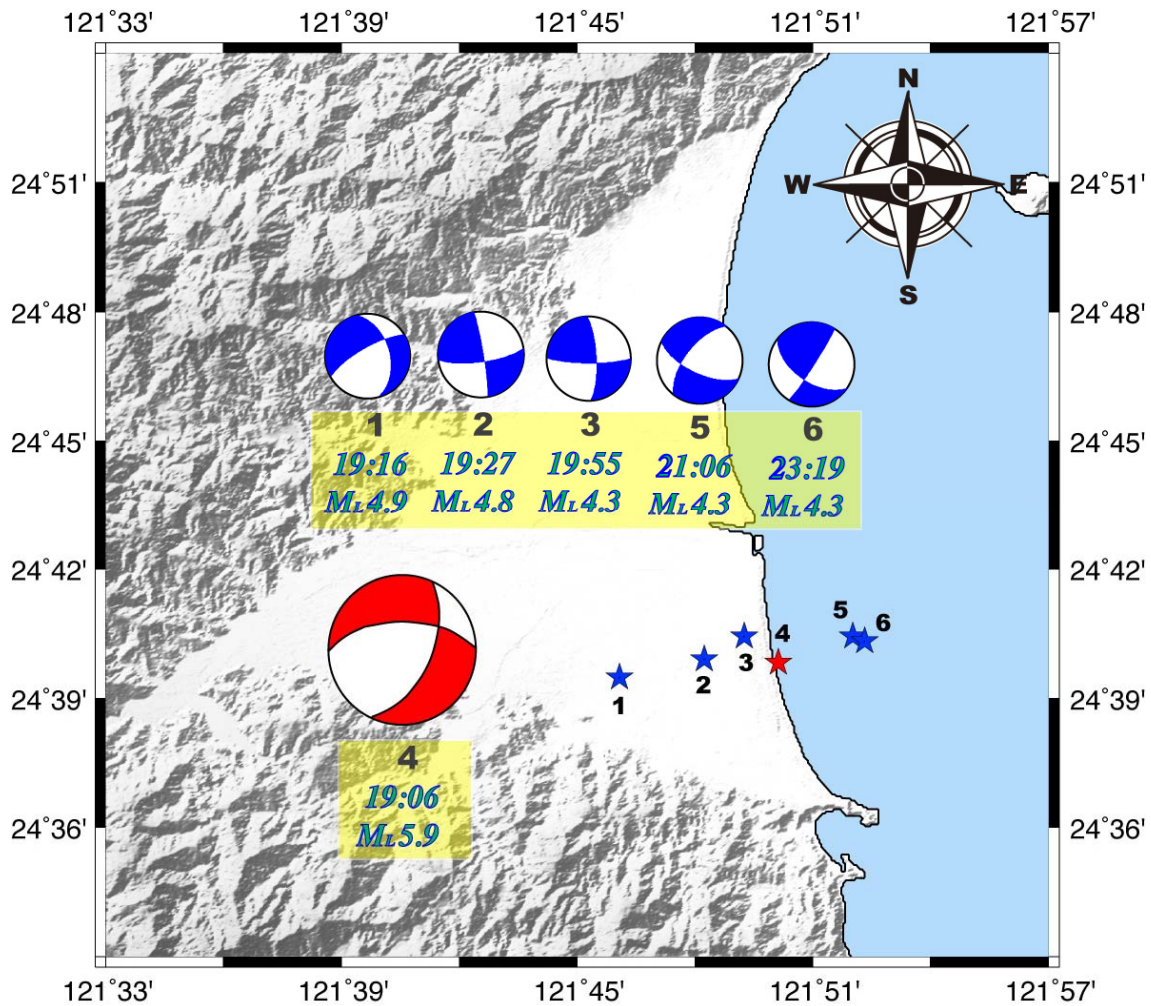


Fig.30 Aftershocks($M_L \geq 4.0$) selected from 5 March, 2005 earthquake cluster, initiated with 19:06 mainshock(No.4) as the seed. Event times were all at date 2005/03/05, and hour and seconds obtained from relocated earthquake catalogue. Magnitude is local magnitude from CWBSN revised announcement. Red star indicates the first mainshock location, and blue stars the aftershocks.

5.4 Physical Interpretation for First Motion and Waveform Inversion

Both first motion method and waveform inversion method are used to determine focal mechanism (e.g., FPFIT by Reasenber and Oppenheimer; Kao et al. 1998b, 1999). Since that only binary up or down from the first arrival counts in first motion method, a dense sampling on the focal sphere and well station-coverage is sufficient. In contrast,

the waveform inversion method may be affected by station coverage, Green's function quality, and frequency used for waveform information. Since complete waveform data is involved in waveform inversion, it must contain complete information of a single event. We could derive from the theory that first motion focal mechanism provides purely initial rupture pattern of the event. On the contrary, waveform inversion method provides average slip motion, depending on the modeled frequency range. Nevertheless, waveform inversion needs to be done under careful control on source, path, and data quality. Therefore there are more uncertainties involved.

By our result on refined P wave first motion and multi-station approach, we can see this event was initially triggered with a normal extension, and later transform to strike-slip. The later motion suggested by aftershocks (Fig. 30) dominates this event as a major pattern. That is why it shows on inversion result as a strike slip pattern. The strike slip motion is well resolved on the wavelength of 0.1~0.3 Hz. Distinct behavior for this single event provide us a vivid example that earthquake rupture changes abruptly during the process, especially at this conjunction of Okinawa opening and southern strike slip pattern. Tsao et al.(2006) applies much time-consuming finite fault method to study this earthquake, but they also indicate initial normal motion as we do.

After this study, the assured concept on focal mechanism determination may help to remind researchers on the physical meaning. Two kinds of results explain

different scale on event rupture duration. Likely, to interpret small scale tectonic, event initiation, or mass statistic of numerous events, first motion is well adequate. But for behavior of the whole rupture, we would suggest inversion result derived from adequate velocity structure and fitting frequency.

5.5 Local Earthquake Characteristics

Distinct physics for different methods suggests us the special earthquake characteristic around the region of Ilan plain. The 5 March, 2005 event is a initially normal-slip motion, by first motion record. Later, this event had still large component on left-lateral strike-slip rupture motion, supported by waveform inversion. We searched through our refined first motion results around this area and compare with BATS inversion CMTs. Eight examples were matched from two methods around Ilan region. This provides us a certain sense of local earthquakes (Fig. 31). There might be three types of earthquake with the same pattern around this location. Some events are of one type resembling 5 March,2005 first mainshock. They initially ruptured as normal, than turned to strike-slip component partially or totally (i.e. events 3~5; Fig. 31).The rest of the events behave consistently from initial to the end (i.e. events 1,2 and 6~8; Fig. 31). Although BATS CMT solutions may have difficulties resolving the normal component around 10 km, it is still evident that rupture pattern changed from initial to

the whole averaged result yielded from waveform inversion. The 5 March, 2005 first mainshock was not alone, but it was relatively a possible, common representative of local earthquakes.

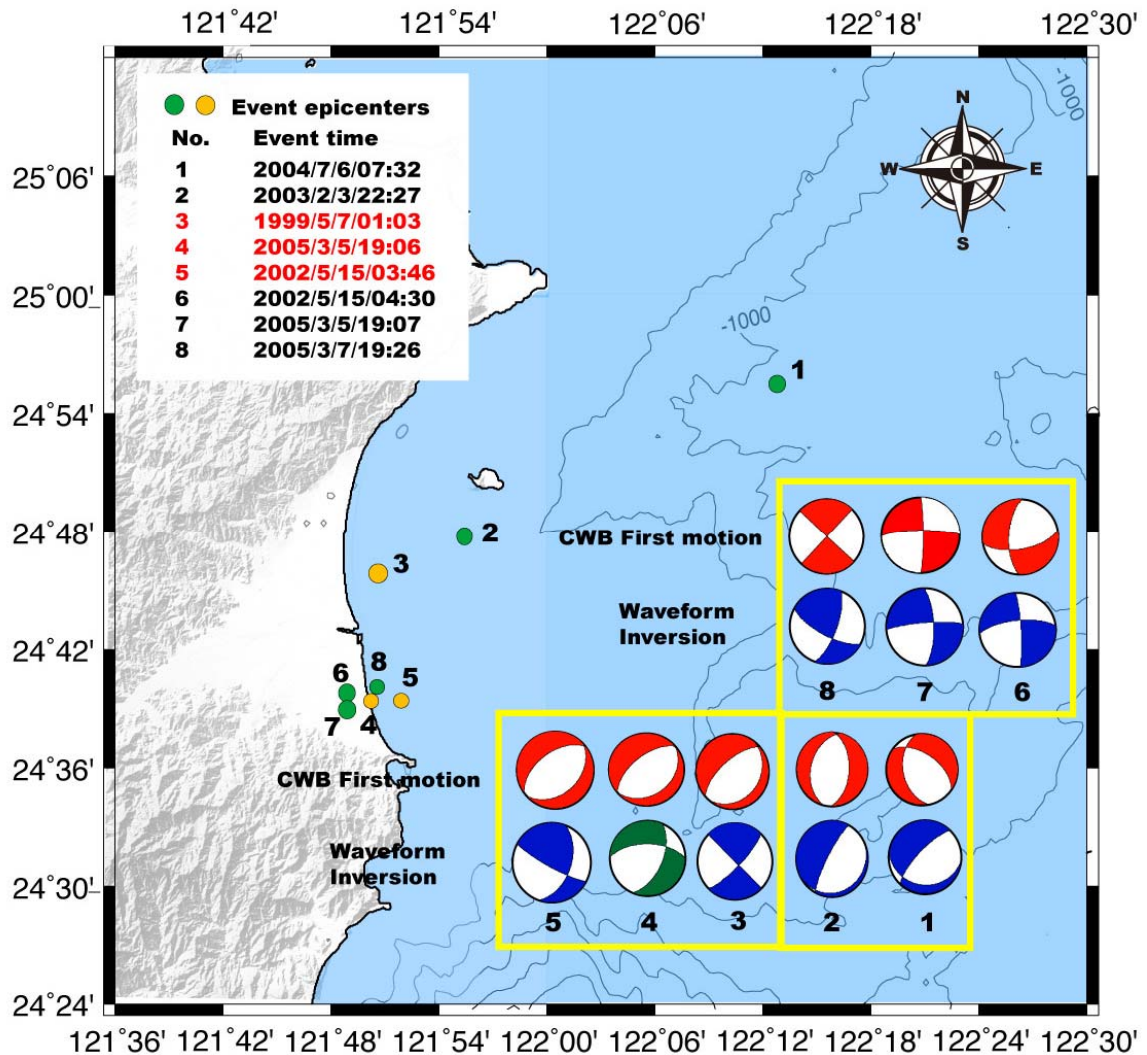


Fig. 31 Eight events matched for two different methods, first motion and waveform inversion. Blue CMTs are BATS solutions, red ones are first motion solutions, and green one is inversion result obtained from this study. Types of Earthquake character are : 1) normal slip turned to strike slip(4-6), 2) strike-slip behaves consistent with strike-slip, and 3) normal behaves consistent with normal. Event 5~9 demonstrate that 5 March, 2005 event might be common characteristic at this location.

6. Conclusions

From the discussion in Chapter 5, we can arrive at the conclusions as following :

1. First motion focal mechanism indicates the initial rupture state of an event, while waveform inversion method responds to the average slip information depending on fitting frequency used.
2. The 5 March 2005 first mainshock was driven by the normal faulting at first, and turned to be left-lateral strike-slip in average, supported by two methods in our study.
3. Single station approach was highly sensitive to severe local velocity structure at Ilan region, even if it can obtain better fitting to observation waveforms.
4. Multi-station approach would assist the moment tensor inversion to obtain a single reliable result.
5. The 5 March, 2005 first mainshock reveal special earthquake character at the location around 121.84°E , 24.66°N , which is not the single case at this region.

REFERENCES

Alekseev, A. S. and B. G. Mikhailenk, (1980) The solution of dynamic problems of elastic wave propagation in inhomogeneous media by a combination of partial separation of variables and finite difference models, *Geophysical Journal*, 48, 161-172.

Angelier, J., T. Y. Chang, J. C. Hu, C. P. Chang, L., Siame, J. C. Lee, B. Deffontaines, T. H. Chu and C. Y. Lu ,(2007) Does extrusion occurs at both tips of the Taiwan collision belt ? Insights from active deformation studies in the Ilan Plain and Pingtung Plain regions. *Tectonophysics*, in revision.

Aki, K., P. G. Richards (1980). *Quantitative Seismology: Theory and Methods*, 1st ed., 932 pp.

Bouchon M., 1981. A simple method to calculate greens functions for elastic layered media. *Bulletin of Seismology Society America*, 71(4), 959-971.

Chen, Y. L. (1995), Three-dimensional velocity structure and kinematic analysis in the Taiwan area. Master Thesis, National Central University. (In Chinese)

Chang, C. H.(2004) Applications of a Dense Seismic Network Data on the Study of Seismogenic Structures of Central and Eastern Taiwan. Doctoral Dissertation, National Central University. (In Chinese)

Chiang, S. C. (1976) Seismic study in the Ilan Plain, *Mining Tech.*, 14(6), 215-221. (In Chinese)

Chou, H. C., Kuo, B. Y., Hung, S. H., Chiao, L. Y., Zhao, D. and Wu, Y. M.(2006) The Taiwan-Ryukyu subduction-collision complex: Folding of a viscoelastic slab and the double seismic zone. *Journal of Geophysical Research*, Vol. 111, B04410, doi:10.1029/2005JB003822

Douglas, H. C. and Larry, J. R. (1985) Analysis of the Trade-off between Hypocentral Depth and Source Time Function. *Bulletin of Seismology Society America*, 75(6), 1637-1656.

Font Y. and Shine L. C.,(2001) Models of the Ongoing Arc-continent Collisional Processes in Taiwan New Insights from Seismic Reflection Analyses and Earthquake Relocation. Doctoral Dissertation, National Taiwan University, Institute of Oceanography.

Gilbert, F. and D. V. Helmberger, (1972) Generalized ray theory for a layered sphere, *Geophysical Journal.*, 27, 57-80.

Haskell, N. A. (1964) Total Energy and Energy Spectral Density of Elastic Wave Radiation from Propagating Faults. *Bulletin of Seismology Society America*, 54(6A), 1811-1841.

Helmberger, D. V. (1974) Generalized ray theory for shear dislocation. *Bulletin of Seismology Society America*, 64(1), 45-64.

Helmberger, D. V. (1974) Generalized ray theory for shear dislocation. *Bulletin of Seismology Society America*, 64(1), 45-64.

Herrmann, R. B., (1979) SH-wave generation by dislocation source – A numerical study. *Bulletin of Seismology Society America*, 69(1), 1-15.

Herrmann, R. B. (2002). *Computer Programs in Seismology, An overview of Synthetic Seismogram Computation.* Version 3.3.0, Appendix I.
<http://www.iasbs.ac.ir/faculty/hamid/askari/herrmann/>

Herrmann, R. B. and Wang, C. Y. (1985): A comparison of synthetic seismograms. *Bulletin of Seismology. Society America*, 75, 41-56.

Ho, C. S. (1988), *An Introduction to the Geology of Taiwan, Explanatory Text of the Geologic Map of Taiwan*, 2nd ed., 192 pp., Cent. Geol. Surv., Taipei.

Huang, B. S. (1994) Estimation of Source Parameters by the Inversion of Near Source Strong Motion Wave Forms. *Terrestrial, Atmospheric and Oceanic Sciences*, Vol. 5, No. 1, 11-26.

Huang, H. S. (2006) The Shallow seismicity in Ilan Region and its Tectonic Implication. Poster on Annual Meeting of Geological Society, 2006.

Jost, M. L. and Herrmann, R. B.,(1989): A Student's Guide to and Review of Moment Tensors. *Seismological Research Letters*, 60, 37-35.

Kao, H., S. J. Shen, and K. F. Ma, (1998b) Transition from oblique subduction to collision: Earthquakes in the southernmost Ryukyu arc-Taiwan region. *Journal of Geophysical Research*, 103, 7211-7229.

Kao, H. and Jian, P. R.(1999). Source Parameters of Regional Earthquakes in Taiwan: July 1995-December 1996. *Terrestrial, Atmospheric and Oceanic Sciences*, Vol. 10, No. 3, 585-604.

Kao, H., Y. H. Liu, W. T. Liang and W. P. Chen (2002). Source Parameters of Regional Earthquakes in Taiwan: 1999-2000 Including the Chi-Chi, Taiwan, Earthquake Sequence. *Terrestrial, Atmospheric and Oceanic Sciences*, Vol. 13, No. 3, 279-298.

Langstan, C. A. and D. V. Helmberger, (1975) A procedure for modeling shallow dislocation sources, *Geophysical Journal* ,42, 117-130.

Liang, W. T., J. C. Lee and B. Y. Kuo (2005). Left-lateral strike-slip faulting in Ilan: Lateral extrusion at the transition between Taiwan mountain range and Okinawa Trough. *Geodynamics and Environment in East Asia International Conference & 5th Taiwan-France Earth Science Symposium*, 104-108.

Liu, K. S., Shin, T. C. and Tsia, Y. B. (1999) A Free-Field Strong Motion Network in Taiwan: TSMIP. *Terrestrial, Atmospheric and Oceanic Sciences*, Vol. 10, No. 2, 377-396.

Lee, C. T., C. T. Cheng, C. W. Liaw, and Y.-B. Chang (1998), Active fault map of Taiwan, Graduate Institute of Applied Geology, Engineering Geology and Advance Technology Lab, Chungli, Taiwan.

Lee, C. Y., Cheng, C. T., Liao, C. W. and Tzai, Y. B. (2001) Site Classification of Taiwan Free-Field Strong-Motion Stations. *Bulletin of Seismology Society America*, 91(5), 1283-1297.

Menke, W. (1989) *Geophysical Data Analysis: Discrete Inverse Theory*, revised ed., Int. Geophys. Series, Academic Press, San Diego, CA. 119-124 pp.

Olson A. H. and R. J. Apsel, (1982) Finite faults and inverse theory with applications to the 1979 Imperial Valley earthquake. *Bulletin of Seismology Society America*, 72(6A), 1969-2001.

Rau, R. J. and Wu, F. T. (1995). Tomographic imaging of lithospheric structures under Taiwan. *Earth Planet. Sci. Lett.*, 133, 517-532.

Satake, K. (1985) Effects of Station Coverage on Moment Tensor Inversion. *Bulletin of Seismology Society America*, 75(6), 1657-1667.

Shyu, J. Bruce H, Kerry Sieh, and Chen, Y. G. (2005), Neotectonic architecture of Taiwan and its implications for future large earthquakes. *Journal of Geophys. Res.*, V. 110, B08402, doi:10.1029/2004JB003251

Silver, P. G. and Jordan, T. H.(1982) Optimal Estimation of Scalar Seismic Moment. *The Geophysical Journal of the Royal Astronomical Society*. 70, 755-787.

Tan, Y., Zhu, L., Helmberger, D. V. and Saikai, C. K. (2006) Locating and modeling regional earthquakes with two stations. *Journal of Geophys. Res.*, V. 111, B01306 doi:10.1029/2005JB003775.

Tsai, Y. B., Teng, T., Chiu, J. M. and Liu, H. L. (1977) Tectonic Implications of the Seismicity in the Taiwan region. *Mem. of the Geology Soc. China*, 2, 13-41.

Tsao, C. W. (2006) Slip distributions of 2005 earthquake doublet beneath I-Lan plain, Taiwan. Master Thesis, National Central University.

Wang, C. (1982) Earthquakes caused by horizontal bending of the Philippine Sea plate near Taiwan. *Tectonophysics*, 88, T1-T6.

Wang, C. Y. and Herrmann, R. B. (1980). A numerical study of *P*-, *SV*-, and *SH*-wave generation in a plane layered medium, *Bulletin of Seismology Society America*, 70, 1015-1036.

Wu, Y. M., C.C. Chen, T.C. Shin, Y.B. Tsai, W.H.K. Lee, and T. L. Teng (1997). Taiwan Rapid Earthquake Information Release System, *Seismological Research Letter*, 68, 931-943.

Wu, Y. M., T. C. Shin, and Y. B. Tsai (1998). Quick and reliable determination of magnitude for seismic early warning, *Bulletin of Seismology Society America*, 88(5), 1254-1259.

Wu, Y. M., J. K. Chung, T. C. Shin, N. C. Hsiao, Y. B. Tsai, W. H. K. Lee, and T. L. Teng (1999). Development of an integrated seismic early warning system in Taiwan-case for Hualien earthquakes. *Terrestrial, Atmospheric and Oceanic Sciences*, 10, 719-736.

Wu, Y. M., Zhao, L. and Chang, C. H. (2007) Focal mechanism determination in Taiwan by genetic algorithm. *Bulletin of Seismology Society America*, in revision.

Wu, F. T. (1978) Recent tectonics of Taiwan. *Journal of Physics of the Earth*, 26(suppl.), S265-S299.

Wu, Y. M., C. H. Chang, L. Zhao, J Bruce H. Shyu, Y. G. Chen, K. Sieh, and J. P. Avouac (2007). Seismic tomography and earthquake relocation in Taiwan using S-P times from a dense network of strong-motion stations. *Journal of Geophys. Res.*, submitted.

Wu, Y. M., N. C. Hsiao, W. H. K. Lee, T. L. Teng, and T. C. Shin (2007). State of the art and progresses of early warning system in Taiwan, in 'Seismic Early Warning' edit by Paolo Gasparini, Gaetano Manfredi, and Jochen Zschau, Springer in press.

Yadav, D. K. and Ma, K. F.(2004) Fault Segmentation and Stress Pattern in North-East Taiwan (Ilan). 2004 Joint Geosciences Assembly(JGA), abstract.

APPENDIX

I. CPS 3.3.0 application flow chart

Referring to kernel code for CPS 3.3.0, download source file at the following website, <http://www.iasbs.ac.ir/faculty/hamid/askari/herrmann>

Explanation to the flow chart is given aside the stencil, and input data description is also added.

STEP	FLOW CHART	DESCRIPTION	INPUT
1		setting appropriate velocity model	layered model
2		intermediate procedure to prepare velocity model for green function generation setting station distance	MODEL (from model96) dfile
3		setting green function	mhspec96.dat (from mhprep96)
4		convolve with source time function	none (flags only)
		displacement waveform or velocity waveform	

P.S. The step 3 and 4 are combined as mhspec.f for a fixed source-time function built-in.

II. TSMIP site and instrument classification

Table 1. Component and polarity conventions of the CWBSC (Seismology Center of Central Weather Bureau) accelerograph.

type	Component			Polarity		
	CH1	CH2	CH3	V	N	E
A800	V	NS	EW	UP	UP	UP
A900	V	NS	EW	UP	UP	UP
A900A	V	NS	EW	UP	UP	UP
IDS-3602	V	NS	EW	UP	UP	DOWN
IDS-3602A	V	NS	EW	UP	UP	DOWN
SSA-16	EW	V	NS	DOWN	DOWN	UP

Green Shaded rows indicates the type of accelerometer record selected in this study

Table 2. Characteristics of six models of accelerographs.

Instrument Model	Manu- facturer	No.	Year of Deploy- ment	Characteristics of Accelerographs				
				Memor- y Size	Record- ing Time	Sampling Rate	Dynamic Range	Real- time Output
A800	Teledyne	52	1991	1 MB	14 Min	200 /s	72 dB	N
A900	Geotech	2	1992	2 MB	27 Min	200 /s	96 dB	N
A900		250	1993	6 MB	87 Min	200 /s	96 dB	N
A900A		150	1994	6.5MB	90 Min	250 /s	96 dB	Y
IDS-3602	Terra Tech	92	1992	2 MB	23 Min	250 /s	96 dB	N
IDS-3602A		100	1994	4 MB	90 Min	250 /s	96 dB	Y
SSA-16	Kinematic	2	1992	2 MB	28 Min	200 /s	96 dB	N

Green Shaded rows indicates the type of accelerometer record selected in this study

III. Bilingual Words and Terminology

English	Chinese	English	Chinese
Ilan	宜蘭	Lanyan	蘭陽
Okinawa	沖繩	Lushan	廬山
Luzon	呂宋	Aoti	澳底
Sansing	三星	Pilushan	畢祿山
Toucheng	頭城	Tananao	大南澳
Suao	蘇澳	Hsitsun	西村
Hsueshan	雪山	Huzhi	鶻子
Ryukyu	琉球	Yijie	隘界
Jaosi	礁溪	Jhoushuei	濁水
Phillipine	菲律賓	Szeleng	四稜
Tatungshan	大桶山	Kengsi	